

Reionization and the Hubble Constant: Correlations in the Cosmic Microwave Background

Itamar J. Allali,^a Praniti Singh,^a JiJi Fan,^{a,b} Lingfeng Li^a

^aDepartment of Physics, Brown University, Providence, RI 02912, USA

^bBrown Theoretical Physics Center, Brown University, Providence, RI 02912, USA

E-mail: itamar_allali@brown.edu, praniti_singh@brown.edu, jiji_fan@brown.edu, lingfeng_li@brown.edu

Abstract. Recently, the James Webb Space Telescope (JWST) has found early galaxies producing photons from more efficient ionization than previously assumed. This may suggest a reionization process with a larger reionization optical depth, τ_{reio} , in some mild disagreement with that inferred from measurements of cosmic microwave background (CMB). Intriguingly, the CMB would prefer larger values of τ_{reio} , more consistent with the recent JWST hint, if the large-scale measurements (i.e. $\ell < 30$) of E-mode polarization are removed. In addition, τ_{reio} has an indirect correlation with today's Hubble constant H_0 in Λ CDM. Motivated by these interesting observations, we investigate and reveal the underlying mechanism for this correlation, using the CMB dataset without the low- ℓ polarization data as a proxy for a potential cosmology with a larger τ_{reio} . We further explore how this correlation may impact the Hubble tension between early and late universe measurements of H_0 , in Λ CDM as well as two proposals to alleviate the Hubble tension: the dark radiation (DR) and early dark energy (EDE) models. We find that the Hubble tension gets further reduced mildly for almost all cases due to the larger τ_{reio} and its positive correlation with H_0 , with either the Baryon Acoustic Oscillations (BAO) data before those from the Dark Energy Spectroscopic Instrument (DESI) or the DESI data.

Contents

1	Introduction	1
2	Cosmological Models and Methods	3
2.1	Cosmological Models	3
2.2	Data Analysis Methods	5
3	Results	5
3.1	$\tau_{\text{reio}}-H_0$ Correlation Within Λ CDM	6
3.2	Data Impact on τ_{reio} and the H_0 Tension	9
3.2.1	Λ CDM	9
3.2.2	Dark Radiation	11
3.2.3	Early Dark Energy	13
4	Conclusion	14
A	Detailed Posterior Statistics	20
A.1	Λ CDM	21
A.2	Dark Radiation	25
A.2.1	FSDR	25
A.2.2	SIDR	29
A.3	Early Dark Energy	33

1 Introduction

A detailed understanding of the epoch of reionization and the “cosmic dawn” is the focus of ongoing and future pursuits, especially the James Webb Space Telescope (JWST) [1, 2]. This time period in the expansion history of the universe marks the ending of the “dark ages,” when the universe was filled with a mostly neutral gas, and the beginning of star and galaxy formation with the reionization of baryonic matter. Astrophysical observatories such as JWST can study this epoch by observing the earliest stars and galaxies, providing insight into the timing and duration of the reionization of the universe. In addition, the cosmic microwave background (CMB), the remnant light from the hot ionized plasma in the early universe and the most precise cosmological probe, provides a test of reionization via the measurement of τ_{reio} , the optical depth of the reionized universe through which the CMB travels to our observatories.

The direct effects of τ_{reio} on the CMB observables are quite straightforward. Long after the CMB is released during the epoch of recombination, the universe undergoes reionization beginning at a redshift $z < 30$ (even as late as $z < 10$, see [3]); CMB photons can be (Thomson) scattered in this reionized universe, slightly scrambling the power spectrum that was encoded at the surface of last scattering. This shows up as an overall suppression of the CMB multipole spectra by a factor of $e^{-2\tau_{\text{reio}}}$ primarily for multipoles $\ell \gtrsim 100$. This effect is almost degenerate with a shift in the overall amplitude of the primordial power spectrum

A_s : the effective amplitude measured in the CMB anisotropies is $A_s e^{-2\tau_{\text{reio}}}$, and thus an increase in either A_s or τ_{reio} can be compensated with an increase in the other. However, the large-scale modes outside the horizon at reionization are less suppressed by τ_{reio} . Modes that cross the horizon during reionization and later ($\ell \lesssim 100$) are subject to less Thomson scattering and thus the power spectrum is less suppressed at these scales. In addition, the Thomson scattering in the late universe has an additional effect on the polarization of the CMB photons, enhancing the E-mode spectra on the largest scales ($\ell \lesssim 10$). These effects break the degeneracy between A_s and τ_{reio} and can serve as an anchor to help determine τ_{reio} more precisely.

The astrophysical approach, on the other hand, serves as an indirect yet independent way of measuring τ_{reio} [4, 5]. The photon rescattering effect is not directly observed in this case, in contrast to the CMB measurement. Instead, the overall τ_{reio} is inferred from the distributions of luminous galaxies, the production rate of ionizing photons in these galaxies, and the chance of their escaping their host galaxies.

The availability of independent means of studying reionization presents an opportunity for confirming our understanding of this epoch or conversely gaining new insight should independent means of measurement disagree. In contrast to the measurement of $\tau_{\text{reio}} = 0.0544 \pm 0.0073$ from the *Planck* satellite’s observations of the CMB [3], recent work suggests a higher τ_{reio} based on JWST data, which could be as high as $\tau_{\text{reio}} \gtrsim 0.07$ (see [6] for various approaches resulting in values of τ_{reio} in this regime). In particular, the increase of τ_{reio} is mainly driven by a higher ionizing efficiency inferred from JWST observations [7, 8], associated with a higher photon production rate at early times. More observed star-forming galaxies at high z also have a subdominant effect in increasing τ_{reio} [9, 10]. Furthermore, several recent surveys in the low- z region [11] indicate a higher escape fraction and imply an even higher $\tau_{\text{reio}} \sim 0.096$ when the result is extrapolated to a higher z .

The studies based on JWST data could be subject to substantial uncertainties from observational bias in galaxy surveys, parameter extrapolation, and baryon physics modeling. See also later discussions [12–15]. On the other hand, the precise determination of τ_{reio} from CMB relies on the large-scale polarization data, which has the largest uncertainties among CMB measurements. Interestingly, Ref. [16] showed that excluding the large-scale CMB data generically predicts a larger value of τ_{reio} . This is more consistent with the value inferred from JWST observations reviewed above.

As these new observations stand to challenge our current picture of reionization, it is important to understand how these measurements may impact other aspects of the standard Λ CDM model of cosmology. In particular, as we will discuss in Section 3.1, the present expansion rate of the universe H_0 has an observed correlation with the value of τ_{reio} when inferred using CMB observations. Given the long-standing tension in the determination of H_0 from CMB observations versus more direct observations of distance ladder methods [17–24], the precise value of τ_{reio} may be of interest. The correlation of these two parameters suggests that an increase in the inferred value of τ_{reio} may alleviate the “Hubble tension.”

In this work, we aim to explore the correlation of τ_{reio} and H_0 and to assess the degree to which this correlation may impact the tension in different measurements of H_0 . In Section 2, we discuss the models that we will study in this work and outline the datasets we consider. Then, in Section 3 we discuss our results. Section 3.1 first covers the physical mechanisms leading to the correlation between H_0 and τ_{reio} when inferred from CMB observations. Then, Section 3.2 gives a detailed discussion of inferred parameters when fitting various models with and without large-scale polarization data from the CMB in order to assess how shifts in τ_{reio}

can impact shifts in H_0 . Finally, in Section 4, we provide a concluding discussion.

2 Cosmological Models and Methods

2.1 Cosmological Models

Throughout this work, we will focus on the following cosmological models.

Λ CDM

The Λ CDM model describes the universe as being composed of radiation, ordinary (baryonic) matter, and cold dark matter (CDM). Additionally, it includes a dark energy component, parameterized by the cosmological constant Λ , which drives the observed accelerated expansion of the universe. In this work we take the universe to be spatially flat.

We parametrize this framework with six major parameters: the Hubble rate of expansion today (Hubble constant) $H_0 = 100 h$ km/s/Mpc, the baryon density $\omega_b = \Omega_b h^2$ (where $\Omega_i \equiv \rho_i/\rho_c$ is the abundance for the i^{th} species, ρ_i its density, and ρ_c the critical energy density for a flat universe today), the cold dark matter density $\omega_{\text{cdm}} = \Omega_{\text{cdm}} h^2$, the scalar spectral index n_s , the amplitude of primordial scalar fluctuations A_s , and the reionization optical depth τ_{reio} . Additionally, in our work, we model the Standard Model (SM) neutrinos as a combination of one massive species with a mass of 0.06 eV and two massless species.

Dark Radiation

We also consider models of dark radiation (DR), additional light degrees of freedom which remain ultra-relativistic until after the epoch of recombination (for a review, see [25]). Thus, in addition to photons and SM neutrinos, the DR component contributes to the radiation density ρ_r . The total relativistic degrees of freedom can be accounted for by the parameter N_{eff} , related to ρ_r as

$$\rho_r = \left[1 + \frac{7}{8} \left(\frac{4}{11} \right)^{4/3} N_{\text{eff}} \right] \rho_\gamma, \quad (2.1)$$

where ρ_γ is the energy density of photons fixed by the CMB temperature. The expression above is defined such that for a single fully thermalized neutrino species, $N_{\text{eff}} = 1$. However, when finite-temperature effects on photons and the non-instantaneous nature of neutrino decoupling are taken into account, the SM predicts $N_{\text{eff}} = 3.044$ [26, 27]. Thus, in the DR model, the contribution of additional relativistic species is parameterized using ΔN_{eff} , defined as:

$$\Delta N_{\text{eff}} \equiv \frac{8}{7} \left(\frac{11}{4} \right)^{4/3} \frac{\rho_{\text{DR}}}{\rho_\gamma}, \quad (2.2)$$

where ρ_{DR} is the energy density of DR.

DR models can help resolve the Hubble tension by leading to a higher H_0 value inferred from CMB data. This is due to the DR's contribution to ρ_r which reduces the size of the sound horizon and thus requires a higher H_0 to preserve its angular size (see e.g. [28, 29]).

Phenomenologically, the ΔN_{eff} parameterization effectively encompasses a broad spectrum of particle physics models. However, the specific microphysical properties of DR can

imprint distinct signatures on cosmological observables. In this work, we investigate two different DR scenarios:

1. Free-Streaming Dark Radiation (FSDR):

In this model, the relativistic species that make up the DR component either do not interact at all with themselves or other species, or have feeble interactions characterized by an interaction rate $\Gamma \ll H$. As a result, these species decouple from the primordial plasma early in the Universe’s history, propagating freely similar to SM neutrinos. The free-streaming property of DR is well motivated by many particle physics models.¹

2. Self-Interacting Dark Radiation (SIDR):

Here, the DR species exhibit strong self-interactions such that their interaction rate $\Gamma \gg H$. This also captures the scenario where Γ is large until after recombination. These interactions inhibit free-streaming, resulting in a suppression of anisotropic stress and viscosity. In this limit, DR behaves as a perfect relativistic fluid, characterized by an equation of state $w = 1/3$. Such self-interaction may stem from various microscopic models such as non-abelian gauge bosons, an interacting light dark sector, or non-standard neutrino interactions with the dark sector (see further discussions in [30–36]).

Early Dark Energy

Another model of interest is the Early Dark Energy (EDE) model [37, 38], which introduces a new component that behaves as dark energy in the early universe and subsequently decays around the time of recombination, effectively injecting energy into the universe at this epoch. This model is typically parameterized by a scalar field, ϕ , with a potential given by $V(\theta) = m^2 f^2 [1 - \cos(\theta)]^n$, where m is the mass of the scalar field, f is its decay constant, $\theta \equiv \phi/f$ and $n \geq 1$ is an integer. Initially, the scalar field is held at a fixed value, θ_i , and behaves as a perfect fluid with an equation of state $w = -1$, keeping its background energy density nearly constant. When the Hubble parameter drops to about $H^2 \sim \partial_\theta^2 V(\theta)/f^2$, the field starts oscillating around the minimum of the potential. Once the oscillations begin around redshift z_c , the EDE component behaves as a fluid with an equation of state $w_n = (n - 1)/(n + 1)$. These oscillations cause the energy density of the field to dilute faster than that of radiation for $n > 2$.

At the background level around recombination, the EDE model is analogous to the DR models: they both inject energy and increase the Hubble expansion parameter, $H(z)$, at that time. The resulting reduction in the sound horizon, r_s , is compensated by decreasing D_A , leading to a higher inferred value of H_0 . The rapid dilution of EDE ensures that its effects are confined to the epoch around recombination, leaving the physics of the late-time universe unaffected.

We parameterize this model using the critical scale factor $a_c = 1/(z_c + 1)$ and the fraction contributed by EDE to the total energy density $f_{\text{EDE}}(z_c)$ at the critical redshift z_c . For our analysis, we fix $n = 3$ and $\theta_i = 2.72$, which are chosen based on the preference of the combined dataset CMB+SH0ES+BAO in [39].

¹As there are many scenarios resulting in dark, light, non-interacting degrees of freedom, we direct the reader to reviews such as [28] for a comprehensive list of candidates.

2.2 Data Analysis Methods

We use CLASS [40, 41] to solve for the cosmological evolution in Λ CDM and DR scenarios, and AxICLASS [42, 43] in the EDE case. We employ Cobaya [44, 45] to perform a Bayesian analysis by generating Markov Chain Monte Carlo (MCMC) samples. Posteriors and plots are obtained using GetDist [46].

To better discuss the impact on τ_{reio} from various data, we consider several combinations of datasets. First, we consider the following to be our “baseline” dataset, against which we make most comparisons:

- \mathcal{B} : CMB data from the *Planck* satellite, including the public release 3 (PR3) likelihoods for the TT and EE power spectra at $\ell < 30$ [47], and the CamSpec likelihood [48] based on the 2020 Planck PR4 data release [49] by [50] for $\ell > 30$ TT, TE, EE data. For CMB lensing, we use the Atacama Cosmology Telescope Data Release 6 (ACT DR6) lensing likelihood [51, 52] combined with the *Planck* PR4 lensing likelihood [53]. We also add the Pantheon+ Type Ia supernovae catalog [54].

As briefly mentioned in the introduction, the CMB constraints on τ_{reio} largely come from the EE spectrum at the largest scales. Thus, to isolate the impact from the low- ℓ EE spectrum, we introduce the modified baseline dataset:

- \mathcal{B}_{EE} : The same as \mathcal{B} but with the EE likelihood for $\ell < 30$ removed.

In addition to CMB and Type Ia supernovae data, we also include measurements of Baryon Acoustic Oscillations (BAO) as an important probe of the cosmological history. In the baseline dataset \mathcal{B} , the BAO data is not specified as the field is under active progress. The differences between BAO datasets are not yet fully understood. In order to ensure our discussion on τ_{reio} is not vulnerable to BAO details, different BAO datasets will be combined with the baseline datasets. We consider the previously accepted set of BAO measurements:

- \mathbf{BAO} : BAO measurements from the 6dF Galaxy Survey (6dFGS) at $z = 0.106$ [55], the Sloan Digital Sky Survey (SDSS) Data Release 7 (DR7) for the main galaxy sample (MGS) at $z = 0.15$ [56], and the CMASS and LOWZ samples of the SDSS BOSS DR12 at redshifts $z = 0.38, 0.51, \text{ and } 0.61$ [57].

Alternatively, we will consider the more recent BAO measurements from the Dark Energy Spectroscopic Instrument (DESI). In particular, the measurements from DESI have shown some preference for larger H_0 and some important impact on resolutions to the Hubble tension (see e.g. [58–66]).

- $\mathbf{BAO}_{\text{DESI}}$: BAO measurements from DESI 2024 for effective redshifts $z = 0.3, 0.51, 0.71, 0.93, 1.32, 1.49, 2.33$ [58].

In the following sections, we will explore the impact of these choices of data on the inferences of τ_{reio} and H_0 .

3 Results

The results of our analysis are discussed below. We begin first by exploring in detail the correlation of τ_{reio} and H_0 in the Λ CDM model. Following that, we present detailed statistics from our analyses of each model discussed, fitting to several datasets. We will make comments on the inferences of τ_{reio} and H_0 , and its impact on the Hubble tension.

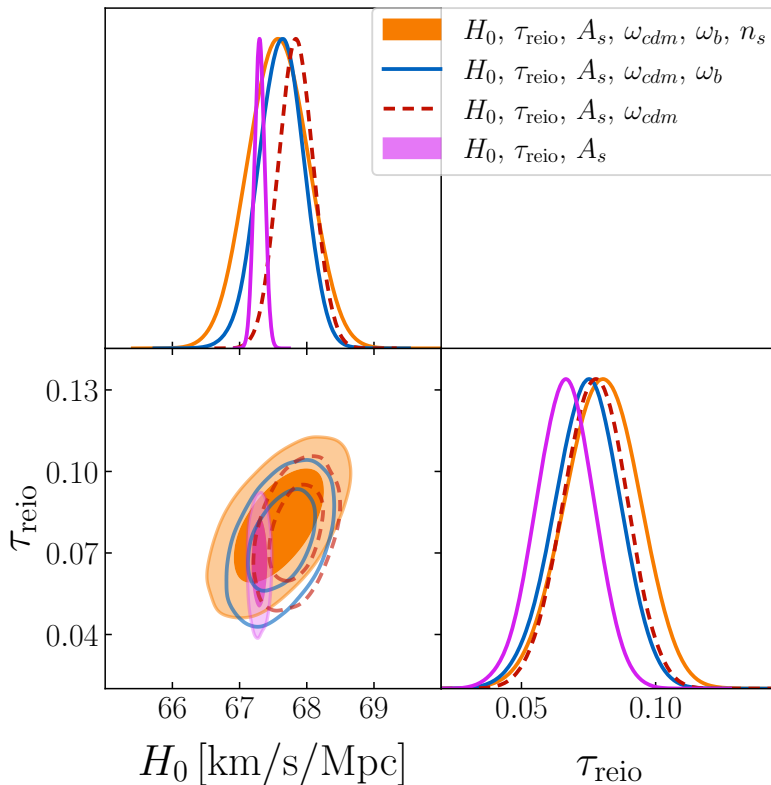


Figure 1: The one- and two-dimensional posterior distributions of H_0 and τ_{reio} in a series of fits to the $\mathcal{B}_{\text{EE}}+\text{BAO}$ dataset. In the purple contour, only three parameters, H_0 , τ_{reio} , and A_s , are allowed to vary. Other cosmological parameters are fixed to *Planck* PR3 best fit values [3] ($\omega_{\text{cdm}} = 0.12011$, $\omega_b = 0.022383$, $n_s = 0.96605$). In this case, H_0 is tightly bounded by the θ_s observable. The fit is followed by the 4-, 5-, and 6-parameter fits by adding ω_{cdm} , ω_b , and n_s as free parameters, respectively. The positive correlation between H_0 and τ_{reio} increases after the inclusion of each parameter, indicating that their correlations are introduced via other cosmological parameters.

3.1 $\tau_{\text{reio}}-H_0$ Correlation Within ΛCDM

In contrast to the direct effects of τ_{reio} on the CMB spectra, the relationship between τ_{reio} and other parameters is not as straightforward. In particular, we are interested in understanding the correlation between the Hubble constant H_0 and τ_{reio} . These two parameters are indirectly correlated, relying on other parameters in ΛCDM . In Figure 1, we show a set of two-dimensional posterior distributions for H_0 and τ_{reio} in the ΛCDM model, fit to the $\mathcal{B}_{\text{EE}}+\text{BAO}$ dataset as defined in Section 2.2, to visualize the correlations.

Figure 1 shows in purple that the inferred values of H_0 and τ_{reio} are uncorrelated when only these two parameters, and the amplitude A_s , are left free to vary. This is partially due to the fact that H_0 is nearly fixed by the angular size of the sound horizon at recombination θ_s , which corresponds to the location of the first peak in the CMB power spectrum, when the total matter density $\omega_m = \Omega_m h^2$ is fixed (see below). Thus, if we allow the cold dark matter density ω_{cdm} to vary, H_0 becomes more variable, and the correlation with τ_{reio} appears. This is seen in Figure 1 in the red dashed contours. We can quantify the correlation by computing

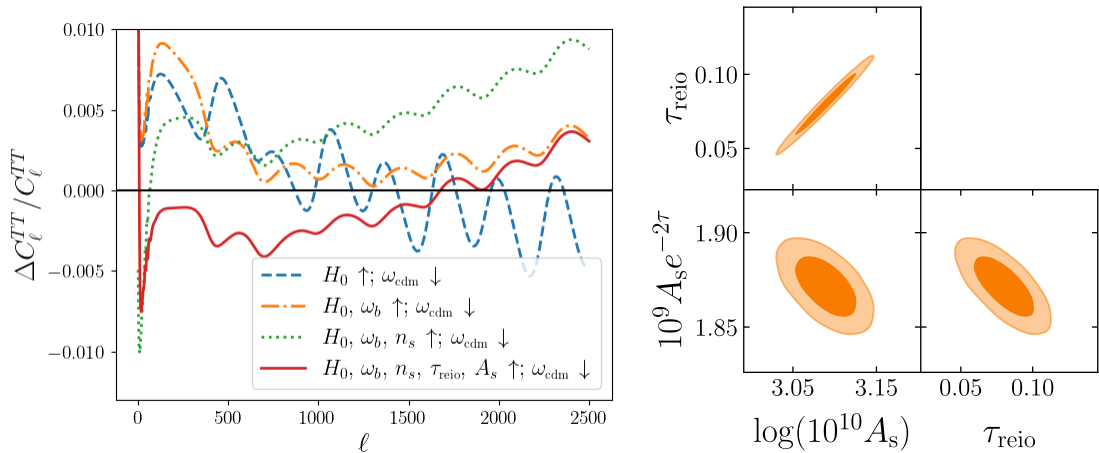


Figure 2: (Left) The relative shift of the CMB TT power spectrum between two benchmark sets of parameters taken from the Monte Carlo sample shown in orange in Figure 1 fit to the $\mathcal{B}_{\text{EE}}+\text{BAO}$ dataset. These two sets of parameters are chosen to highlight the shift in H_0 , and both have a nearly minimal effective χ^2 and thus represent cosmologies that fit the data reasonably well. The parameters are given in Table 1. In the legends, \uparrow indicates parameters increased with respect to the initial choice, while \downarrow indicates a decrease.

(Right) Two-dimensional posterior distributions of $\{\tau_{\text{reio}}, A_s, A_s e^{-2\tau_{\text{reio}}}\}$ from the 6-parameter fit to the $\mathcal{B}_{\text{EE}}+\text{BAO}$ dataset depicted in Figure 1. The tight correlation of τ_{reio} and A_s necessitates their simultaneous shift, while their anticorrelation with the effective CMB amplitude $A_s e^{-2\tau_{\text{reio}}}$ indicates that a simultaneous increase of A_s and τ_{reio} results in a suppression of the CMB power spectrum, as in the red curve of the left panel.

the Pearson correlation coefficient $R(H_0, \tau_{\text{reio}})$ (the ratio of the parameters' covariance to the product of their standard deviations). For the case of the 4-parameter fit, $R(H_0, \tau_{\text{reio}}) = 0.34$. Adding the baryon density ω_b as a free parameter allows for an even greater variation of H_0 without significantly enhancing the correlation with $R(H_0, \tau_{\text{reio}}) = 0.38$. Finally, adding the final free parameter of ΛCDM , n_s , also adds to the degree of correlation, giving the orange filled contours in Figure 1 and $R(H_0, \tau_{\text{reio}}) = 0.57$. Note that the data that results in these correlations excludes the low- ℓ EE CMB data, which allows for a greater range of τ_{reio} and aids in understanding the correlation. In fact, as we will explore in the remainder of this section, the effects driving this correlation can be understood via primarily the TT part of the CMB power spectrum at $\ell > 30$, and fitting to this data alone gives an even stronger correlation of $R(H_0, \tau_{\text{reio}}) = 0.75$. In Section 3.2, we explore other effects of the datasets further.

Let us now explore how the correlation between H_0 and τ_{reio} comes about from the variation of other parameters. First, in order to increase H_0 while keeping the angular size of the sound horizon θ_s the same, we must decrease ω_m in the flat ΛCDM model. One can compute this scale directly from the values of $H_0 = 100h$ km/s/Mpc and $\omega_m = \Omega_m h^2$, given by the ratio of the sound horizon at recombination r_s and the angular diameter distance to the surface of last scattering D_A

$$\theta_s = \frac{r_s}{D_A} = \frac{\int_{z_{\text{rec}}}^{\infty} c_s dz / H(z)}{\int_0^{z_{\text{rec}}} c dz / H(z)}, \quad (3.1)$$

where c_s is the speed of sound in the early universe (dependent on ω_b), z_{rec} is the redshift of recombination, and $H(z)$ is given by the Friedmann equation

$$H^2(z) = (100 \text{ km/s/Mpc})^2 [\omega_r(1+z)^4 + \omega_m(1+z)^3 + h^2 - \omega_m - \omega_r]. \quad (3.2)$$

Note that the radiation abundance $\omega_r = \Omega_r h^2$ is relatively fixed in Λ CDM by the CMB temperature and the number of neutrinos. An increase in H_0 for fixed ω_m keeps r_s virtually unchanged, while decreasing D_A ; thus, a decrease in ω_m is needed to increase D_A and leave θ_s unchanged.

Increasing H_0 and decreasing ω_m both induce opposite phase shifts (by shifting the primary peak location corresponding to θ_s) in the CMB spectra, which nearly cancel. However, some major deformations of the spectrum remain. First, there is a leftover enhancement of the CMB spectrum in the vicinity of the first peak, around $\ell \sim 200$. This change can be seen in the blue dashed curve in the left panel of Figure 2, depicting the residual change in the multipole coefficients C_ℓ of the TT power spectrum when increasing H_0 and decreasing ω_{cdm} with respect to a reference choice of parameters (given in Table 1). With a decrease in ω_m , the time of matter-radiation equality is delayed, resulting in two reasons for an enhancement of the primary peak: (i) there is less time during matter-domination prior to recombination for modes crossing the horizon around that time to be damped; and (ii) the early integrated Sachs-Wolfe (EISW) effect is enhanced because the metric potentials have less time to settle to their constant values, further enhancing the peak (see [67] for more details). Another deformation to the spectrum caused by the shift in H_0 and ω_{cdm} is a residual phase shift due to the relative heights of even and odd peaks in the power spectrum. This can be compensated by shifting the baryon abundance ω_b , as shown in the orange dot-dashed curve of the left panel in Figure 2.

Parameters	H_0 [km/s/Mpc]	ω_{cdm}	ω_b	n_s	A_s	τ_{reio}
Unmodified	67.4	0.1193	0.02218	0.9632	2.21×10^{-9}	0.083
Modified	68.1	0.1179	0.02234	0.9672	2.25×10^{-9}	0.095

Table 1: The parameters before and after the modifications corresponding to the curves in the left panel of Figure 2; the power spectrum difference from shifting all of these parameters at once is given by the red curve.

With the phase of the peaks mostly restored, we are still left with an increase in the CMB anisotropy power at $\ell < 500$ at around the percent level. This could be somewhat corrected by an increase in τ_{reio} which suppresses the power spectrum, explaining the very mild correlation in the four- and five-parameter fits of Figure 1. However, since the largest enhancement of power remains at smaller ℓ , this introduces an effective red tilt to the power spectrum residuals (higher power at large scales/small ℓ); thus τ_{reio} , which suppresses power nearly democratically at most scales, cannot compensate directly. Instead, one can increase the spectral index n_s , which controls precisely the tilt of the power spectrum, introducing a relative blue tilt (shifting the already red tilt closer to scale invariance). This effect is shown in the green dotted curve of the left panel in Figure 2, pushing down the TT residual for the largest scales (smallest ℓ). Now, an increase in τ_{reio} is appropriate to suppress the power spectrum. In practice, the fit to data prefers both an increase in τ_{reio} and A_s , corresponding to the red curve in Figure 2 with residuals well below the percent level down to $\ell < 30$. The initial and final sets of parameters, resulting in the red residual curve, are given in Table 1.

We want to comment more on the last step above in which the data prefer to raise both τ_{reio} and A_s simultaneously, instead of shifting only one of these two nearly degenerate parameters. Examining the contours in the right panel of Figure 2, from the same analysis as in Figure 1, we observe the correlations between A_s , τ_{reio} , and the effective amplitude measured in the CMB $A_s e^{-2\tau_{\text{reio}}}$. First, one notices the very tight correlation between τ_{reio} and A_s . Since the effective amplitude of the CMB is measured relatively precisely, shifting τ_{reio} necessitates shifting A_s to restore the measured value of $A_s e^{-2\tau_{\text{reio}}}$; thus, both parameters must shift in unison. Then, after shifting H_0 , ω_{cdm} , ω_b , and n_s , one is left with an overall enhanced power spectrum with respect to the initial benchmark. Figure 2 shows that achieving this suppression is possible with an increase in A_s and τ_{reio} , as evidenced by their anticorrelation with the effective amplitude.

We can therefore appreciate that the correlation between H_0 and τ_{reio} within the flat Λ CDM model crucially involves the other parameters in the model. Having established the mechanism for this correlation, we wish to understand the impact that an increase in τ_{reio} could have on inferences of H_0 and the Hubble tension, as explored in the remainder of this work.

3.2 Data Impact on τ_{reio} and the H_0 Tension

We will focus on constraints for $\{H_0, \tau_{\text{reio}}\}$, as our aim is to examine the role of inferences of τ_{reio} in determining the value of H_0 and consequently the Hubble tension. Since the removal of large-scale polarization data results in an increase in the inferred value of τ_{reio} , we will make a comparison between fitting to the \mathcal{B} and the \mathcal{B}_{EE} datasets to assess the impact of such an increase. In each case, we combine with either **BAO** or **BAO_{DESI}**.

We present the complete results of our analyses in Appendix A for all models and dataset combinations discussed above. In addition to the analyzing $\mathcal{B} + \mathbf{BAO}$ and $\mathcal{B}_{\text{EE}} + \mathbf{BAO}$ datasets, we also extend our investigation to include the SH0ES measurement of H_0 [17], see Appendix A for more details. For each analysis, we provide posterior distributions and 68% C.L. intervals for all six cosmological parameters $\{A_s, n_s, \tau_{\text{reio}}, H_0, \omega_{\text{cdm}}, \omega_b\}$, along with new physics parameters for both the DR and EDE models, in Appendix A. Furthermore, we provide best-fit values of these parameters along with the corresponding χ^2 values for the different likelihoods used in our analyses in Appendix A.

3.2.1 Λ CDM

Figure 3 shows posteriors of $\{H_0, \tau_{\text{reio}}\}$ in Λ CDM, and their allowed ranges at 68% C.L. are listed in Table 2. As discussed in the previous sections, for modes within the horizon at reionization, corresponding to $\ell \gtrsim 100$, the power spectrum is suppressed by a factor $e^{-2\tau_{\text{reio}}}$ and the associated data only depends on the combination $A_s e^{-2\tau_{\text{reio}}}$. This degeneracy is broken by the low- ℓ data, in particular, the polarization measurements. Thus, from Figure 3, we can see that τ_{reio} is more constrained in the presence of low- ℓ EE CMB spectra data (solid contours). Without the low- ℓ ($\ell < 30$) EE CMB spectra, there could be more variation in τ_{reio} with a larger mean value, as well as a stronger correlation between τ_{reio} and H_0 . This correlation is indirect and arises through an involved interplay with other cosmological parameters, as discussed in detail in Section 3.1. We also provide in Table 2 the Pearson correlation coefficient between H_0 and τ_{reio} denoted as $R(H_0, \tau_{\text{reio}})$.

Table 2 also lists the Gaussian tension when comparing the values of H_0 in our runs with the SH0ES measurement $(H_0)_{\text{SH0ES}} = 74.03$ km/s/Mpc with its standard deviation,

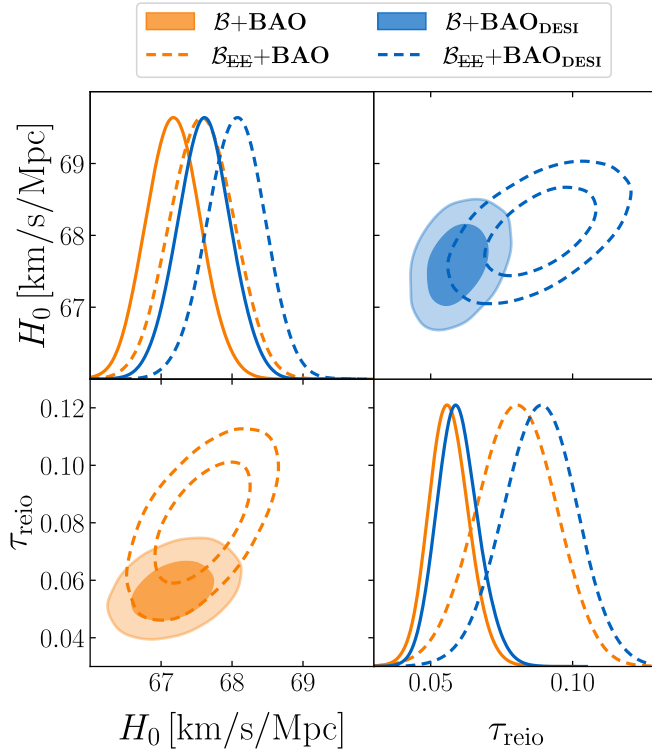


Figure 3: Posterior distributions of H_0 and τ_{reio} in ΛCDM . The results from the **BAO** dataset are shown in the lower-left part of the plot as orange contours. In the upper-right corner, results from the **BAO_{DESI}** dataset are shown in blue. Solid curves and filled contours represent fits to the \mathcal{B} dataset, while dashed curves/contours represent the outcome from the \mathcal{B}_{EE} dataset. The **BAO_{DESI}** dataset tends to have higher H_0 and τ_{reio} central values than the **BAO** dataset, with their correlations similar in both cases. Removing the low- ℓ EE data significantly shifts the central values of τ_{reio} and enlarges the corresponding uncertainties. The central values and uncertainties of H_0 also increase, though less significantly.

$\sigma_{\text{SHOES}} = 1.04 \text{ km/s/Mpc}$ [17]. The Gaussian tension for a given run is calculated as:

$$(\Delta H_0)_{\text{GT}} = \frac{|H_0 - (H_0)_{\text{SHOES}}|}{\sqrt{\sigma^2 + \sigma_{\text{SHOES}}^2}}, \quad (3.3)$$

where H_0 is the mean value and σ the standard deviation from the MCMC analysis. One can see that for a given BAO dataset, without the low- ℓ polarization data, the Hubble tension is mildly alleviated, thanks to the larger τ_{reio} and its positive correlation with H_0 .

It has already been shown that using the DESI BAO measurements tends to enhance the value of H_0 [58–66]. Here we also show our results for runs with $\mathcal{B}+\text{BAO}_{\text{DESI}}$, observing slightly higher preferred values for both τ_{reio} and H_0 . Furthermore, upon removing the low- ℓ EE data, these parameters shift to even higher values, and the Hubble tension is reduced down to 4.5σ when fit to $\mathcal{B}_{\text{EE}}+\text{BAO}_{\text{DESI}}$. Moreover, for both **BAO** and **BAO_{DESI}** runs, we find that the correlation between τ_{reio} and H_0 remains nearly the same, with $R(H_0, \tau_{\text{reio}}) = 0.58$ for $\mathcal{B}_{\text{EE}}+\text{BAO}$ and $R(H_0, \tau_{\text{reio}}) = 0.53$ for $\mathcal{B}_{\text{EE}}+\text{BAO}_{\text{DESI}}$.

	$\mathcal{B}+\text{BAO}$	$\mathcal{B}_{\text{EE}}+\text{BAO}$	$\mathcal{B}+\text{BAO}_{\text{DESI}}$	$\mathcal{B}_{\text{EE}}+\text{BAO}_{\text{DESI}}$
τ_{reio}	$0.0565^{+0.0066}_{-0.0074}$	0.080 ± 0.014	$0.0596^{+0.0066}_{-0.0078}$	0.088 ± 0.013
H_0 [km/s/Mpc]	67.18 ± 0.38	67.58 ± 0.44	67.60 ± 0.37	68.05 ± 0.40
$R(H_0, \tau_{\text{reio}})$	0.34	0.58	0.34	0.53
H_0 Tension	5.3σ	4.8σ	4.9σ	4.5σ

Table 2: The posterior central values and corresponding 68% C.L. intervals from the Λ CDM model, fitting to four different datasets. The Pearson correlation coefficient $R(H_0, \tau_{\text{reio}})$ is given. All H_0 tension values are obtained from the Gaussian approximation in Eq. (3.3).

3.2.2 Dark Radiation

An interesting feature of DR models is their potential to alleviate the H_0 tension, as the presence of DR results in a higher inferred value of H_0 compared to Λ CDM. The contribution of DR to ω_r leads to an increase in the expansion rate $H(z)$ through Eq. (3.2) at early times before recombination. Consequently, this increase in $H(z)$ reduces the sound horizon, r_s , at recombination. Thus, to maintain the angular size of the sound horizon, $\theta_s = r_s/D_A$, a higher value of H_0 , which decreases D_A , is needed.

Posteriors for the key parameters $\{H_0, \tau_{\text{reio}}, \Delta N_{\text{eff}}\}$ for both the FSDR and SIDR models are shown in Figure 4, with 68% C.L. constraints for $\{H_0, \tau_{\text{reio}}\}$ and 95% C.L. upper bounds for ΔN_{eff} presented in Table 3. We provide the 95% C.L. upper bounds for any parameter which does not generate a credible 68% C.L. interval away from zero. From Figure 4, we can see the expected strong correlation between H_0 and ΔN_{eff} for all four runs based on different combinations of datasets, due to the relatively fixed angular sound horizon scale θ_s . For τ_{reio} , both DR models exhibit a behavior similar to that observed in the Λ CDM model (see Section 3.2.1): τ_{reio} is less constrained and tends to favor a higher value in the absence of low- ℓ EE CMB data. While H_0 and τ_{reio} are still correlated after removing the low- ℓ EE data (for similar reasons as discussed in Section 3.1), the strength of this correlation is now reduced, compared to those in Λ CDM model (see Table 3). The reduction in correlations can be understood as follows: the shift in H_0 , ΔN_{eff} , ω_{cdm} , ω_b , and n_s that is induced in this scenario leaves the CMB power spectra overall suppressed, rather than mostly enhanced as in the case of Λ CDM (see Section 3.1), with the strongest suppression at the lowest $\ell \lesssim 100$. Thus, an increase in A_s is warranted to restore the power spectrum. A further increase in

	FSDR		SIDR	
	$\mathcal{B}+\text{BAO}$	$\mathcal{B}_{\text{EE}}+\text{BAO}$	$\mathcal{B}+\text{BAO}$	$\mathcal{B}_{\text{EE}}+\text{BAO}$
τ_{reio}	0.0566 ± 0.0071	0.078 ± 0.014	0.0570 ± 0.0071	0.081 ± 0.014
H_0 [km/s/Mpc]	$68.13^{+0.58}_{-0.92}$	$68.45^{+0.60}_{-0.91}$	$68.14^{+0.59}_{-0.94}$	$68.69^{+0.69}_{-1.1}$
$R(H_0, \tau_{\text{reio}})$	0.17	0.27	0.23	0.35
ΔN_{eff} (95% C.L.)	< 0.376	< 0.370	< 0.340	< 0.380
H_0 Tension	4.1σ	3.8σ	4.1σ	3.5σ

Table 3: The posterior mean values and corresponding 68% C.L. intervals for SIDR and FSDR models for parameters $\{H_0, \tau_{\text{reio}}\}$, along with H_0 tension values. For the new physics parameter ΔN_{eff} , the 95% C.L. upper limits are presented instead. The Pearson correlation coefficient $R(H_0, \tau_{\text{reio}})$ is also given.

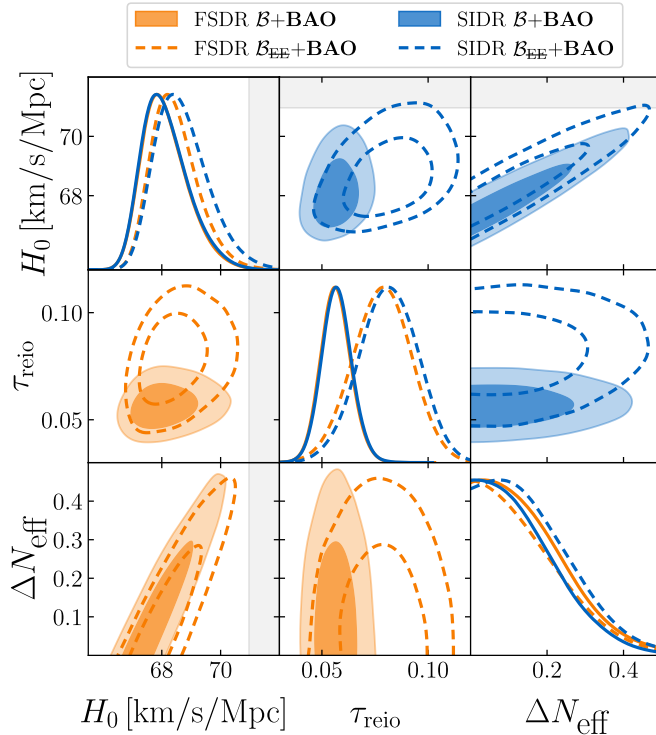


Figure 4: Posterior distributions of H_0 , τ_{reio} and ΔN_{eff} in DR models. The orange (blue) contours represent the free-streaming (self-interacting) scenario. Solid curves and filled contours represent fits to the \mathcal{B} dataset, while dashed curves/contours represent the outcome from \mathcal{B}_{EE} dataset. The gray shaded area shows the 2σ range of H_0 from the SH0ES measurement. Similar to Figure 3, removing the low- ℓ EE data makes the central values and uncertainties of τ_{reio} and H_0 larger. However, compared to the Λ CDM case, the correlation between H_0 and τ_{reio} is weakened in both DR models.

τ_{reio} can be combined with the enhancement from A_s so that the power is enhanced more at $\ell \lesssim 100$ than above, which nearly restores the power spectrum at all ℓ .

Both DR models yield similar constraints with the full CMB dataset. Yet the SIDR model exhibits a preference for slightly larger values of both τ_{reio} and H_0 in the absence of the low- ℓ CMB EE data compared to the FSDR model. Moreover, as expected, even with the low- ℓ EE measurements included, both models already favor slightly higher values of H_0 due to extra energy injection from additional relativistic species, i.e. $\Delta N_{\text{eff}} > 0$. Removing the low- ℓ EE polarization data further amplifies this preference, thereby providing a moderately improved alleviation of the H_0 tension. This is also reflected in the reduction in the Gaussian tensions shown in the last line of Table 3, once the low- ℓ EE data is removed.

The results for the DR models with **BAO_{DES}** runs are reported in Appendix A.2. Similar to the Λ CDM results, we see slightly higher preferred values for both H_0 and τ_{reio} . As shown previously in the literature [59], SIDR has the potential to resolve the Hubble tension if the DESI results are confirmed in future releases, and thus this scenario is of interest. See Appendix A.2 for more details.

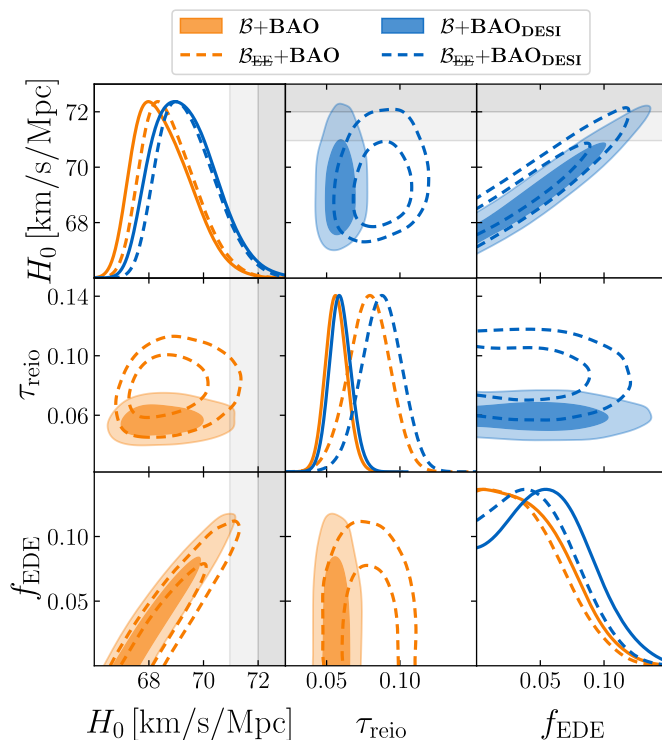


Figure 5: Posterior distributions of H_0 , τ_{reio} and f_{EDE} in EDE models. The orange (blue) contours represent fits to the **BAO** (**BAO_{DESI}**) dataset. Solid curves and filled contours represent fits to the \mathcal{B} dataset, while dashed curves/contours represent the outcome from \mathcal{B}_{EE} dataset. The gray shaded area shows the 1σ (dark gray) and 2σ (light gray) range of H_0 from the SH0ES measurement. Similar to Figure 3, removing the low- ℓ EE data makes the central value and uncertainties of τ_{reio} larger, while not for H_0 . However, compared to the Λ CDM case, the correlation between H_0 and τ_{reio} is significantly weakened.

3.2.3 Early Dark Energy

Here, posteriors of the parameters $\{H_0, \tau_{\text{reio}}, f_{\text{EDE}}\}$ are shown in Figure 5, with their 68% C.L. constraints presented in Table 4 for both the \mathcal{B} and \mathcal{B}_{EE} datasets combined with both **BAO** and **BAO_{DESI}**. We provide the 95% C.L. upper bounds for any parameter which does not generate a credible 68% C.L. interval away from zero. First, we see a strong correlation between f_{EDE} and H_0 as expected. Since the EDE model is known to alleviate the H_0 tension, we observe a significant relaxation in the H_0 tension both with and without the low- ℓ EE polarization data. In particular, with the DESI BAO data, the H_0 tension is relaxed further compared to the results with earlier BAO data. For each choice of the BAO data, excluding the low- ℓ polarization data does not vary the level of Hubble tension significantly.

As observed in previous models, we find that τ_{reio} is less constrained, with higher values preferred when low- ℓ EE CMB spectral data are excluded. However, unlike previous models, we observe that even without the low- ℓ EE polarization data, the positive correlation between τ_{reio} and H_0 remains quite insignificant (see Table 4). This is likely due to the fact that the increase in H_0 in the EDE model is mainly driven by f_{EDE} . Thus, an increase in τ_{reio} could not help further increase H_0 , which is consistent with the roughly constant Gaussian tension for a given BAO dataset, as reported in Table 4.

	$\mathcal{B}+\mathbf{BAO}$	$\mathcal{B}_{\text{EE}}+\mathbf{BAO}$	$\mathcal{B}+\mathbf{BAO}_{\text{DESI}}$	$\mathcal{B}_{\text{EE}}+\mathbf{BAO}_{\text{DESI}}$
τ_{reio}	0.0566 ± 0.0073	0.079 ± 0.014	$0.0594^{+0.0069}_{-0.0077}$	0.087 ± 0.014
H_0 [km/s/Mpc]	$68.52^{+0.77}_{-1.2}$	$68.78^{+0.74}_{-1.2}$	$69.32^{+0.92}_{-1.3}$	$69.43^{+0.80}_{-1.2}$
$R(H_0, \tau_{\text{reio}})$	0.11	0.22	0.10	0.18
f_{EDE}	< 0.0977	< 0.0924	$0.056^{+0.028}_{-0.041}$	$0.048^{+0.016}_{-0.045}$
H_0 Tension	3.5σ	3.3σ	2.7σ	2.8σ

Table 4: The posterior mean values and corresponding 68% C.L. intervals for the EDE model for parameters $\{H_0, \tau_{\text{reio}}, f_{\text{EDE}}\}$ along with its H_0 tension values. For f_{EDE} , the 95% C.L. upper bounds are provided only when a credible 68% interval away from zero is not obtained. The Pearson correlation coefficient $R(H_0, \tau_{\text{reio}})$ is also given.

4 Conclusion

In this work, we have explored the correlation between the cosmological parameters τ_{reio} and H_0 in the context of Λ CDM cosmology and beyond. We have drawn on three motivations to guide this endeavor:

(1) Since its launch, JWST has been providing an unprecedented sensitivity to directly probe the properties of the first galaxies. Early observations reveal that faint, early galaxies were efficient producers of ionizing photons, with likely non-negligible escape fractions, suggesting an excess in the ionizing-photon budget during the epoch of reionization. These observations hint at a larger value of τ_{reio} than that inferred from the CMB.

(2) The CMB constraints on τ_{reio} mainly come from E-mode polarization data at large scales, i.e., $\ell \lesssim 30$, by breaking the measurement degeneracy between A_s and τ_{reio} . Previously, [16] showed that the CMB tends to prefer larger values of τ_{reio} when large-scale measurements are excluded.

(3) There is an indirect correlation in the CMB data between inferences of τ_{reio} and H_0 . Therefore, since a shift in τ_{reio} arising from either motivation (1) or (2) above could impact the inferred value of H_0 according to (3), we have investigated the nature of this correlation and have analyzed to what extent it can be informative for the Hubble Tension.

First, as expected, the absence of low- ℓ E-mode polarization data allows for greater variations in τ_{reio} across all three models we have studied. We observe a shift of approximately $1.4-2\sigma$ in each case. In the Λ CDM model, this increased variation in τ_{reio} allows for a stronger positive correlation between τ_{reio} and H_0 . This correlation still exists but is weaker in the DR models compared to Λ CDM. In the EDE model, however, the correlation almost disappears.

For Λ CDM, as a result of the preference for larger values of τ_{reio} without large scale E-mode polarization data, we find that the Hubble tension gets reduced by a slight shift from 5.3σ to 4.8σ when combined with the **BAO** dataset and 4.5σ with the **BAO_{DESI}** dataset. While the DR and EDE models already mitigate the Hubble tension when the low- ℓ E-mode polarization data is included, we find that the tension is further reduced when excluding this dataset for almost all cases (except for the EDE model fit with the DESI BAO data).

To further contextualize our findings, a few concluding comments are in order:

- As emphasized in [16], the EE signal constraining the precise value of τ_{reio} is at the scales where the limit on the precision is set by cosmic variance, thus making results highly sensitive to even small unknown systematics. However, we do not claim to have

any evidence against the low- ℓ EE dataset. Rather, we use the CMB dataset without the low- ℓ EE data as a proxy to study a potential cosmology with a larger τ_{reio} .

- There are some other potential concerns on the large-scale polarization data [16]. Galactic foregrounds impact polarization anisotropies and can introduce potential errors if poorly understood. In addition, anomalies persist in temperature and polarization anisotropies at large scales including features in the TT and TE spectra at low multipoles ($\ell \lesssim 10$).
- Since the CMB EE and TE spectra at low multipoles could be significantly influenced by τ_{reio} , precise measurements of these spectra can provide a clearer picture on τ_{reio} and reionization physics. Future CMB missions such as LiteBIRD [68], ECHO [69, 70] and PICO [71] will be able to measure polarization across large scales, providing even tighter constraints on τ_{reio} . In addition, ground-based experiments such as Simons Observatory (SO) [72], POLARBEAR [73], and BICEP3-Keck array [74] will provide complementary observations at smaller scales leading to a more complete picture of the CMB. Moreover, Large Scale Structure (LSS) surveys by missions such as Euclid [75] can also break A_s and τ_{reio} degeneracy by providing a more precise constraint on A_s .
- The precise astrophysical determination of τ_{reio} is still under development, relying on multiple surveys across a range of z . The validity of the conclusion also depends on extrapolations of known results. With further observations from JWST, the preferred range of τ_{reio} may change. Moreover, parallel approaches such as Lyman- α forest [76–79] and 21-cm tomography [80, 81] could reveal the history of reionization, further examining the consistency of cosmology.

Our results have explored the relationship between two important parameters of cosmology, both studied actively by many collaborations. Future observations of the late universe may lead to a clearer prediction of τ_{reio} . In concert, upcoming CMB polarization experiments will provide the most precise inferences of τ_{reio} possible. As such, we have provided a road map for understanding the impact of τ_{reio} on H_0 and for interpreting any further shifts in measurements of reionization or the Hubble constant from observations outside of the CMB.

Acknowledgements

We thank Nils Schöneberg and Julian Muñoz for useful discussions. IJA, JF, LL and PS are supported by the NASA grant 80NSSC22K081 and the DOE grant DE-SC-0010010. This work was conducted using computational resources and services at the Center for Computation and Visualization, Brown University.

References

- [1] P. Jakobsen, P. Ferruit, C. Alves de Oliveira, S. Arribas, G. Bagnasco, R. Barho et al., *The Near-Infrared Spectrograph (NIRSpec) on the James Webb Space Telescope. I. Overview of the instrument and its capabilities*, *Astron. Astrophys.* **661** (2022) A80 [2202.03305].
- [2] G.S. Wright, G.H. Rieke, A. Glasse, M. Ressler, M. García Marín, J. Aguilar et al., *The Mid-infrared Instrument for JWST and Its In-flight Performance*, *Publ. Astron. Soc. Pac.* **135** (2023) 048003.

- [3] PLANCK collaboration, *Planck 2018 results. VI. Cosmological parameters*, *Astron. Astrophys.* **641** (2020) A6 [1807.06209].
- [4] B.E. Robertson, R.S. Ellis, S.R. Furlanetto and J.S. Dunlop, *Cosmic Reionization and Early Star-forming Galaxies: a Joint Analysis of new Constraints From Planck and the Hubble Space Telescope*, *Astrophys. J. Lett.* **802** (2015) L19 [1502.02024].
- [5] M. McQuinn, *The Evolution of the Intergalactic Medium*, *Ann. Rev. Astron. Astrophys.* **54** (2016) 313 [1512.00086].
- [6] J.B. Muñoz, J. Mirocha, J. Chisholm, S.R. Furlanetto and C. Mason, *Reionization after JWST: a photon budget crisis?*, *Mon. Not. Roy. Astron. Soc.* **535** (2024) L37 [2404.07250].
- [7] C. Simmonds, S. Tacchella, K. Hainline, B.D. Johnson, W. McClymont, B. Robertson et al., *Low-mass bursty galaxies in JADES efficiently produce ionizing photons and could represent the main drivers of reionization*, *Mon. Not. R. Astron. Soc.* **527** (2024) 6139 [2310.01112].
- [8] R. Endsley, D.P. Stark, L. Whitler, M.W. Topping, B.D. Johnson, B. Robertson et al., *The star-forming and ionizing properties of dwarf z 6-9 galaxies in JADES: insights on bursty star formation and ionized bubble growth*, *Mon. Not. R. Astron. Soc.* **533** (2024) 1111 [2306.05295].
- [9] S.L. Finkelstein, M.B. Bagley, H.C. Ferguson, S.M. Wilkins, J.S. Kartaltepe, C. Papovich et al., *CEERS Key Paper. I. An Early Look into the First 500 Myr of Galaxy Formation with JWST*, *Astrophys. J. Lett.* **946** (2023) L13 [2211.05792].
- [10] S.L. Finkelstein, G.C.K. Leung, M.B. Bagley, M. Dickinson, H.C. Ferguson, C. Papovich et al., *The Complete CEERS Early Universe Galaxy Sample: A Surprisingly Slow Evolution of the Space Density of Bright Galaxies at $z \sim 8.5$ – 14.5* , *Astrophys. J. Lett.* **969** (2024) L2 [2311.04279].
- [11] J. Chisholm, A. Saldana-Lopez, S. Flury, D. Schaerer, A. Jaskot, R. Amorín et al., *The far-ultraviolet continuum slope as a Lyman Continuum escape estimator at high redshift*, *Mon. Not. R. Astron. Soc.* **517** (2022) 5104 [2207.05771].
- [12] P. Mukherjee, A. Dey and S. Pal, *What can we learn about Reionization astrophysical parameters using Gaussian Process Regression?*, **2407.19481**.
- [13] D. Paoletti, D.K. Hazra, F. Finelli and G.F. Smoot, *The asymmetry of dawn: evidence for asymmetric reionization histories from a joint analysis of cosmic microwave background and astrophysical data*, **2405.09506**.
- [14] Y. Zhu et al., *SMILES: Discovery of Higher Ionizing Photon Production Efficiency in Overdense Regions*, **2410.14804**.
- [15] C. Cain, G. Lopez, A. D’Aloisio, J.B. Munoz, R.A. Jansen, R.A. Windhorst et al., *Chasing the beginning of reionization in the JWST era*, **2409.02989**.
- [16] W. Giarè, E. Di Valentino and A. Melchiorri, *Measuring the reionization optical depth without large-scale CMB polarization*, *Phys. Rev. D* **109** (2024) 103519 [2312.06482].
- [17] A.G. Riess et al., *A Comprehensive Measurement of the Local Value of the Hubble Constant with $1 \text{ km s}^{-1} \text{ Mpc}^{-1}$ Uncertainty from the Hubble Space Telescope and the SH0ES Team*, *Astrophys. J. Lett.* **934** (2022) L7 [2112.04510].
- [18] L. Breuval, A.G. Riess, S. Casertano, W. Yuan, L.M. Macri, M. Romaniello et al., *Small Magellanic Cloud Cepheids Observed with the Hubble Space Telescope Provide a New Anchor for the SH0ES Distance Ladder*, *Astrophys. J.* **973** (2024) 30 [2404.08038].
- [19] D. Scolnic, A.G. Riess, J. Wu, S. Li, G.S. Anand, R. Beaton et al., *CATS: The Hubble Constant from Standardized TRGB and Type Ia Supernova Measurements*, *Astrophys. J. Lett.* **954** (2023) L31 [2304.06693].

- [20] A.G. Riess et al., *JWST Validates HST Distance Measurements: Selection of Supernova Subsample Explains Differences in JWST Estimates of Local H_0* , *Astrophys. J.* **977** (2024) 120 [2408.11770].
- [21] H0LiCOW collaboration, *H0LiCOW – XIII. A 2.4 per cent measurement of H_0 from lensed quasars: 5.3 σ tension between early- and late-Universe probes*, *Mon. Not. Roy. Astron. Soc.* **498** (2020) 1420 [1907.04869].
- [22] W.L. Freedman, B.F. Madore, I.S. Jang, T.J. Hoyt, A.J. Lee and K.A. Owens, *Status Report on the Chicago-Carnegie Hubble Program (CCHP): Three Independent Astrophysical Determinations of the Hubble Constant Using the James Webb Space Telescope*, 2408.06153.
- [23] W.L. Freedman and B.F. Madore, *Progress in direct measurements of the Hubble constant*, *JCAP* **11** (2023) 050 [2309.05618].
- [24] W.L. Freedman, *Measurements of the Hubble Constant: Tensions in Perspective*, *Astrophys. J.* **919** (2021) 16 [2106.15656].
- [25] M. Archidiacono, E. Giusarma, S. Hannestad and O. Mena, *Cosmic dark radiation and neutrinos*, *Adv. High Energy Phys.* **2013** (2013) 191047 [1307.0637].
- [26] J. Froustey, C. Pitrou and M.C. Volpe, *Neutrino decoupling including flavour oscillations and primordial nucleosynthesis*, *JCAP* **12** (2020) 015 [2008.01074].
- [27] J.J. Bennett, G. Buldgen, P.F. De Salas, M. Drewes, S. Gariazzo, S. Pastor et al., *Towards a precision calculation of N_{eff} in the Standard Model II: Neutrino decoupling in the presence of flavour oscillations and finite-temperature QED*, *JCAP* **04** (2021) 073 [2012.02726].
- [28] E. Di Valentino, O. Mena, S. Pan, L. Visinelli, W. Yang, A. Melchiorri et al., *In the realm of the Hubble tension—a review of solutions*, *Class. Quant. Grav.* **38** (2021) 153001 [2103.01183].
- [29] N. Schöneberg, G. Franco Abellán, A. Pérez Sánchez, S.J. Witte, V. Poulin and J. Lesgourgues, *The H_0 Olympics: A fair ranking of proposed models*, *Phys. Rept.* **984** (2022) 1 [2107.10291].
- [30] K.S. Jeong and F. Takahashi, *Self-interacting Dark Radiation*, *Phys. Lett. B* **725** (2013) 134 [1305.6521].
- [31] M.A. Buen-Abad, G. Marques-Tavares and M. Schmaltz, *Non-Abelian dark matter and dark radiation*, *Phys. Rev. D* **92** (2015) 023531 [1505.03542].
- [32] M.A. Buen-Abad, M. Schmaltz, J. Lesgourgues and T. Brinckmann, *Interacting Dark Sector and Precision Cosmology*, *JCAP* **01** (2018) 008 [1708.09406].
- [33] C. Brust, Y. Cui and K. Sigurdson, *Cosmological Constraints on Interacting Light Particles*, *JCAP* **08** (2017) 020 [1703.10732].
- [34] N. Blinov and G. Marques-Tavares, *Interacting radiation after Planck and its implications for the Hubble Tension*, *JCAP* **09** (2020) 029 [2003.08387].
- [35] T. Brinckmann, J.H. Chang, P. Du and M. LoVerde, *Confronting interacting dark radiation scenarios with cosmological data*, *Phys. Rev. D* **107** (2023) 123517 [2212.13264].
- [36] M.A. Buen-Abad, Z. Chacko, I. Flood, C. Kilic, G. Marques-Tavares and T. Youn, *Atomic Dark Matter, Interacting Dark Radiation, and the Hubble Tension*, 2411.08097.
- [37] T. Karwal and M. Kamionkowski, *Dark energy at early times, the Hubble parameter, and the string axiverse*, *Phys. Rev. D* **94** (2016) 103523 [1608.01309].
- [38] V. Poulin, T.L. Smith, T. Karwal and M. Kamionkowski, *Early Dark Energy Can Resolve The Hubble Tension*, *Phys. Rev. Lett.* **122** (2019) 221301 [1811.04083].
- [39] T.L. Smith, V. Poulin and M.A. Amin, *Oscillating scalar fields and the hubble tension: A resolution with novel signatures*, *Physical Review D* **101** (2020) .

- [40] D. Blas, J. Lesgourgues and T. Tram, *The cosmic linear anisotropy solving system (class). part ii: Approximation schemes*, *JCAP* **2011** (2011) 034–034.
- [41] J. Lesgourgues, *The cosmic linear anisotropy solving system (class) i: Overview*, 2011.
- [42] T.L. Smith, V. Poulin and M.A. Amin, *Oscillating scalar fields and the Hubble tension: a resolution with novel signatures*, *Phys. Rev. D* **101** (2020) 063523 [1908.06995].
- [43] V. Poulin, T.L. Smith, D. Grin, T. Karwal and M. Kamionkowski, *Cosmological implications of ultralight axionlike fields*, *Phys. Rev. D* **98** (2018) 083525 [1806.10608].
- [44] J. Torrado and A. Lewis, “Cobaya: Bayesian analysis in cosmology.” Astrophysics Source Code Library, record ascl:1910.019, Oct., 2019.
- [45] J. Torrado and A. Lewis, *Cobaya: Code for Bayesian Analysis of hierarchical physical models*, *JCAP* **05** (2021) 057 [2005.05290].
- [46] A. Lewis, *Getdist: a python package for analysing monte carlo samples*, 2019.
- [47] PLANCK collaboration, *Planck 2018 results. V. CMB power spectra and likelihoods*, *Astron. Astrophys.* **641** (2020) A5 [1907.12875].
- [48] G. Efstathiou and S. Gratton, *A detailed description of the camspec likelihood pipeline and a reanalysis of the planck high frequency maps*, *The Open Journal of Astrophysics* **4** (2021) .
- [49] PLANCK collaboration, *Planck intermediate results. LVII. Joint Planck LFI and HFI data processing*, *Astron. Astrophys.* **643** (2020) A42 [2007.04997].
- [50] E. Rosenberg, S. Gratton and G. Efstathiou, *Cmb power spectra and cosmological parameters from planck pr4 with camspec*, *Mon. Not. Roy. Astron. Soc.* **517** (2022) 4620–4636.
- [51] ACT collaboration, *The Atacama Cosmology Telescope: A Measurement of the DR6 CMB Lensing Power Spectrum and Its Implications for Structure Growth*, *Astrophys. J.* **962** (2024) 112 [2304.05202].
- [52] ACT collaboration, *The Atacama Cosmology Telescope: DR6 Gravitational Lensing Map and Cosmological Parameters*, *Astrophys. J.* **962** (2024) 113 [2304.05203].
- [53] J. Carron, M. Mirmelstein and A. Lewis, *CMB lensing from Planck PR4 maps*, *JCAP* **09** (2022) 039 [2206.07773].
- [54] D. Scolnic et al., *The Pantheon+ Analysis: The Full Data Set and Light-curve Release*, *Astrophys. J.* **938** (2022) 113 [2112.03863].
- [55] F. Beutler, C. Blake, M. Colless, D.H. Jones, L. Staveley-Smith, L. Campbell et al., *The 6df galaxy survey: baryon acoustic oscillations and the local hubble constant: 6dfgs: Baos and the local hubble constant*, *Mon. Not. Roy. Astron. Soc.* **416** (2011) 3017–3032.
- [56] A.J. Ross, L. Samushia, C. Howlett, W.J. Percival, A. Burden and M. Manera, *The clustering of the SDSS DR7 main Galaxy sample – I. A 4 per cent distance measure at $z = 0.15$* , *Mon. Not. Roy. Astron. Soc.* **449** (2015) 835 [1409.3242].
- [57] BOSS collaboration, *The clustering of galaxies in the completed SDSS-III Baryon Oscillation Spectroscopic Survey: cosmological analysis of the DR12 galaxy sample*, *Mon. Not. Roy. Astron. Soc.* **470** (2017) 2617 [1607.03155].
- [58] DESI collaboration, *DESI 2024 VI: Cosmological Constraints from the Measurements of Baryon Acoustic Oscillations*, **2404.03002**.
- [59] I.J. Allali, A. Notari and F. Rompineve, *Dark Radiation with Baryon Acoustic Oscillations from DESI 2024 and the H_0 tension*, **2404.15220**.
- [60] F.J. Qu, K.M. Surrao, B. Bolliet, J.C. Hill, B.D. Sherwin and H.T. Jense, *Accelerated inference on accelerated cosmic expansion: New constraints on axion-like early dark energy with DESI BAO and ACT DR6 CMB lensing*, **2404.16805**.

- [61] H. Wang and Y.-S. Piao, *Dark energy in light of recent DESI BAO and Hubble tension*, [2404.18579](#).
- [62] O. Seto and Y. Toda, *DESI constraints on the varying electron mass model and axionlike early dark energy*, *Phys. Rev. D* **110** (2024) 083501 [[2405.11869](#)].
- [63] G.P. Lynch, L. Knox and J. Chluba, *DESI observations and the Hubble tension in light of modified recombination*, *Phys. Rev. D* **110** (2024) 083538 [[2406.10202](#)].
- [64] J.-Q. Jiang, D. Pedrotti, S.S. da Costa and S. Vagnozzi, *Non-parametric late-time expansion history reconstruction and implications for the Hubble tension in light of recent DESI and Type Ia supernovae data*, [2408.02365](#).
- [65] A. Chatrchyan, F. Niedermann, V. Poulin and M.S. Sloth, *Confronting cold new early dark energy and its equation of state with updated CMB, supernovae, and BAO data*, *Phys. Rev. D* **111** (2025) 043536 [[2408.14537](#)].
- [66] Y.-Z. Li and J.-H. Yu, *Neutrinophilic Λ CDM Extension for EMPRESS, DESI and Hubble Tension*, [2501.13153](#).
- [67] J. Lesgourgues, *Cosmological Perturbations*, in *Theoretical Advanced Study Institute in Elementary Particle Physics: Searching for New Physics at Small and Large Scales*, pp. 29–97, 2013, DOI [[1302.4640](#)].
- [68] LITEBIRD collaboration, *LiteBIRD: JAXA’s new strategic L-class mission for all-sky surveys of cosmic microwave background polarization*, *Proc. SPIE Int. Soc. Opt. Eng.* **11443** (2020) 114432F [[2101.12449](#)].
- [69] A. Sen, S. Basak, T. Ghosh, D. Adak and S. Sinha, *Importance of high-frequency bands for removal of thermal dust in ECHO*, *Phys. Rev. D* **108** (2023) 083529 [[2212.02869](#)].
- [70] D. Adak, A. Sen, S. Basak, J. Delabrouille, T. Ghosh, A. Rotti et al., *B-mode forecast of CMB-Bhārat*, *Mon. Not. Roy. Astron. Soc.* **514** (2022) 3002 [[2110.12362](#)].
- [71] NASA PICO collaboration, *PICO: Probe of Inflation and Cosmic Origins*, [1902.10541](#).
- [72] SIMONS OBSERVATORY collaboration, *The Simons Observatory: Science goals and forecasts*, *JCAP* **02** (2019) 056 [[1808.07445](#)].
- [73] POLARBEAR collaboration, *POLARBEAR-2: an instrument for CMB polarization measurements*, *Proc. SPIE Int. Soc. Opt. Eng.* **9914** (2016) 99141I [[1608.03025](#)].
- [74] L. Moncelsi et al., *Receiver development for BICEP Array, a next-generation CMB polarimeter at the South Pole*, *Proc. SPIE Int. Soc. Opt. Eng.* **11453** (2020) 1145314 [[2012.04047](#)].
- [75] L. Amendola et al., *Cosmology and fundamental physics with the Euclid satellite*, *Living Rev. Rel.* **21** (2018) 2 [[1606.00180](#)].
- [76] M. Ouchi, Y. Ono and T. Shibuya, *Observations of the Lyman- α Universe*, *Ann. Rev. Astron. Astrophys.* **58** (2020) 617 [[2012.07960](#)].
- [77] Z. Chen, D.P. Stark, C. Mason, M.W. Topping, L. Whitler, M. Tang et al., *JWST spectroscopy of z 5–8 UV-selected galaxies: new constraints on the evolution of the Ly α escape fraction in the reionization era*, *Mon. Not. R. Astron. Soc.* **528** (2024) 7052 [[2311.13683](#)].
- [78] M. Nakane, M. Ouchi, K. Nakajima, Y. Harikane, Y. Ono, H. Umeda et al., *Ly α Emission at $z = 7–13$: Clear Evolution of Ly α Equivalent Width Indicating a Late Cosmic Reionization History*, *Astrophys. J.* **967** (2024) 28 [[2312.06804](#)].
- [79] T.-Y. Lu, C.A. Mason, A. Hutter, A. Mesinger, Y. Qin, D.P. Stark et al., *The reionizing bubble size distribution around galaxies*, *Mon. Not. Roy. Astron. Soc.* **528** (2024) 4872 [[2304.11192](#)].
- [80] M.F. Morales and J.S.B. Wyithe, *Reionization and Cosmology with 21-cm Fluctuations*, *Annu. Rev. Astron. Astrophys.* **48** (2010) 127 [[0910.3010](#)].

- [81] HERA collaboration, *HERA Phase I Limits on the Cosmic 21 cm Signal: Constraints on Astrophysics and Cosmology during the Epoch of Reionization*, *Astrophys. J.* **924** (2022) 51 [2108.07282].
- [82] KILO-DEGREE SURVEY, DES collaboration, *DES Y3 + KiDS-1000: Consistent cosmology combining cosmic shear surveys*, *Open J. Astrophys.* **6** (2023) 2305.17173 [2305.17173].

A Detailed Posterior Statistics

We provide the posterior distributions of all cosmological parameters for various models and datasets discussed previously. Additionally, we present analyses including the local measurement of H_0 , using Cepheid-calibrated supernova distances, by the SH0ES collaboration. For this dataset, which we will denote \mathbf{H}_0 , we use the implementation in `Cobaya` denoted “pantheonplusshoes” which replaces the Pantheon+ dataset in \mathcal{B} with a new Pantheon+ dataset calibrated using the intrinsic Type Ia supernova brightness $M_b = -19.253 \pm 0.027$, as reported by the SH0ES collaboration [17].

Appendix A.1 covers the Λ CDM model, with posterior distributions plotted in Figures 6 and 7 and marginalized statistics in Tables 5 and 6. In addition, we obtain best-fit parameters for each analysis via likelihood maximization, utilizing once more the `Cobaya` sampler. Tables 7 and 8 provide the best-fit parameter values while Tables 9 and 10 provide the minimized effective χ^2 for each likelihood. Shorthand notations for the likelihood names in `Cobaya` are given in Table 29. Subsequently, Appendix A.2 covers the DR models, with FSDR model depicted in Figures 8 and 9 and Tables 11 to 16, while SIDR results are shown in Figures 10 and 11 and Tables 17 to 22. Finally, Appendix A.3 covers the EDE model via Figures 12 and 13 and Tables 23 to 28.

Let us comment briefly on the impact of our analysis on the value of the matter clustering parameter $S_8 = \sigma_8 \sqrt{\Omega_m}/0.3$. There is a mild tension between measurements of this parameter by weak lensing surveys and the inferred value from fitting Λ CDM to CMB data. The status of this tension is unclear, since, for example, the combination of the KiDS-1000 and DES Y3 datasets yields a mild 1.7σ disagreement with CMB observations [82]. Yet, it is important to assess this tension in scenarios with increasing τ_{reio} and increasing H_0 as these parameters are known to make the S_8 tension worse.² In our analysis, we observe that S_8 is slightly increased with the removal of low- ℓ EE data. However, the tension remains $\lesssim 2.5\sigma$ in each analysis we presented for Λ CDM and the DR models. For EDE, which is known to increase S_8 , the tension still remains below 3σ without the low- ℓ EE data.

²We thank David Spergel for pointing out the increase of S_8 as a result of increasing τ_{reio} .

A.1 Λ CDM

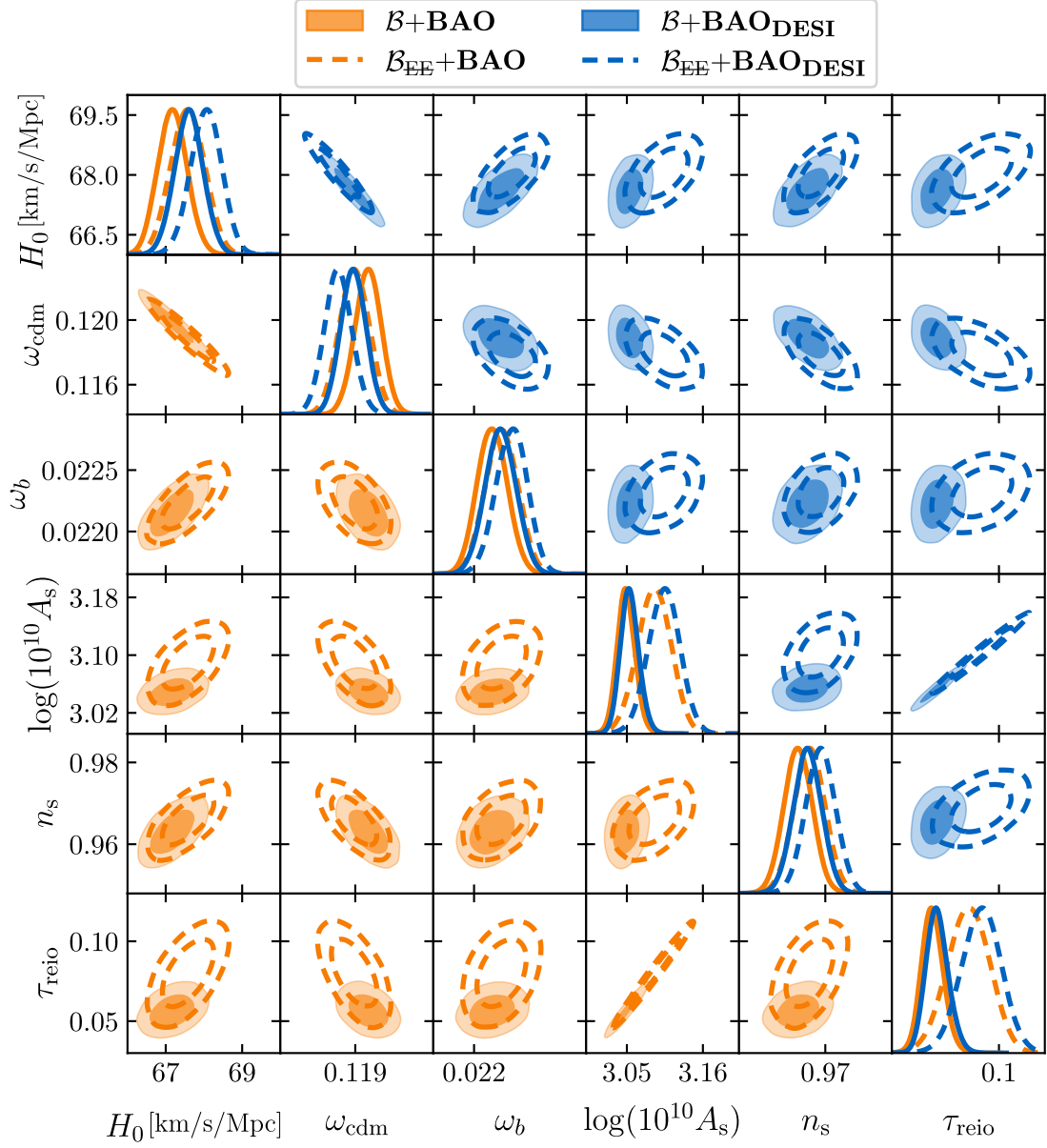


Figure 6: Posterior distributions of the cosmological parameters in the Λ CDM model. The results from the **BAO** (**BAO_{DESI}**) dataset are shown in the lower-left (upper-right) part of the plot as orange (blue) contours. Solid (dashed) contours represent the results obtained from the \mathcal{B} (\mathcal{B}_{EE}) dataset.

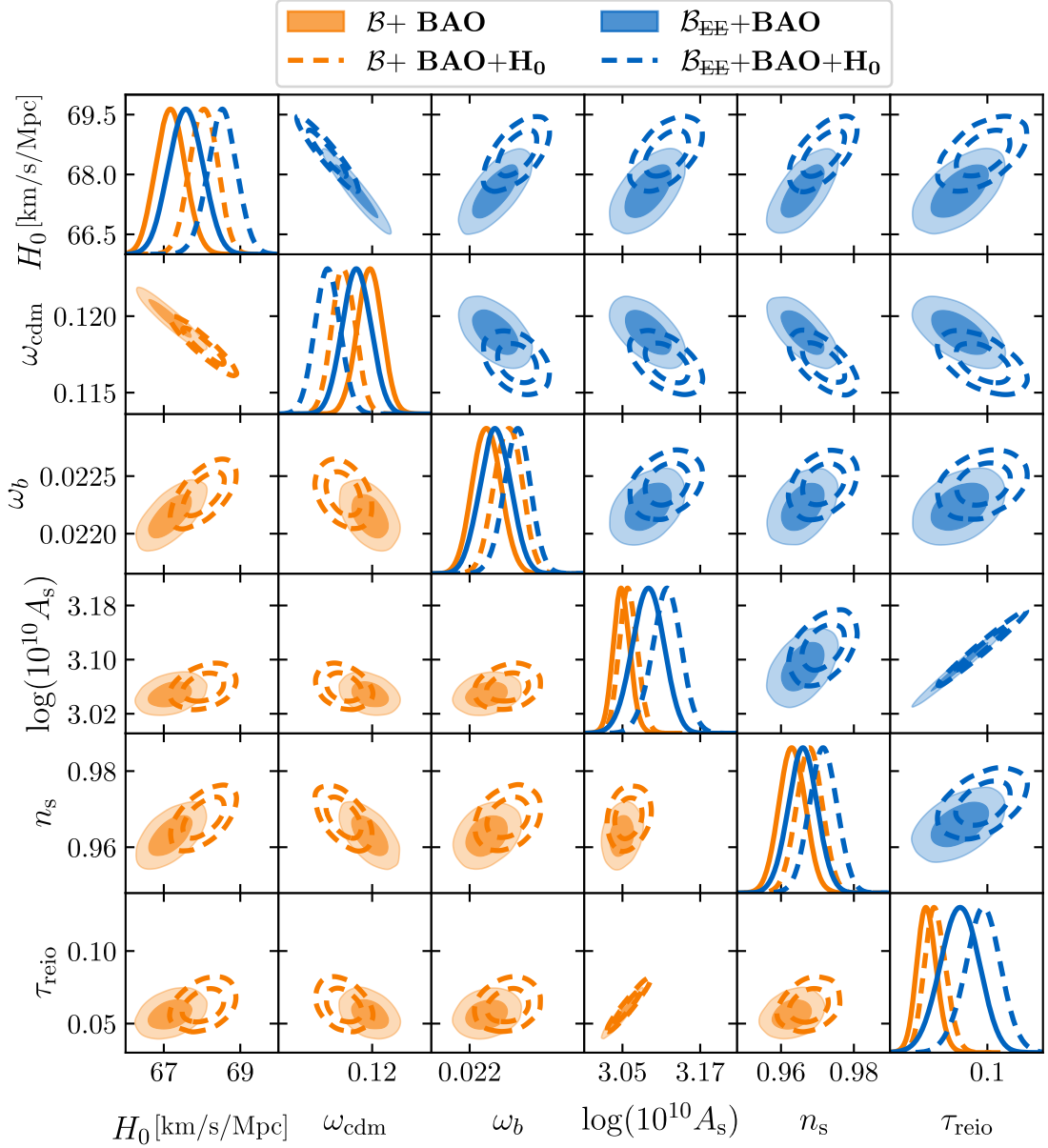


Figure 7: Posterior distributions of the cosmological parameters in the Λ CDM model. The orange (blue) contours show the $\mathcal{B}+\text{BAO}$ ($\mathcal{B}_{\text{EE}}+\text{BAO}$) dataset. In dashed contours, the \mathbf{H}_0 dataset is included, pulling the posteriors to the high H_0 region.

	$\mathcal{B}+\mathbf{BAO}$	$\mathcal{B}_{\mathbf{EE}}+\mathbf{BAO}$	$\mathcal{B}+\mathbf{BAO}_{\mathbf{DES}}\mathbf{I}$	$\mathcal{B}_{\mathbf{EE}}+\mathbf{BAO}_{\mathbf{DES}}\mathbf{I}$
$\log(10^{10} A_s)$	3.049 ± 0.013	3.089 ± 0.024	$3.054^{+0.012}_{-0.014}$	3.104 ± 0.023
n_s	0.9631 ± 0.0036	0.9660 ± 0.0040	0.9655 ± 0.0036	0.9688 ± 0.0038
τ_{reio}	$0.0565^{+0.0066}_{-0.0074}$	0.080 ± 0.014	$0.0596^{+0.0066}_{-0.0078}$	0.088 ± 0.013
H_0 [km/s/Mpc]	67.18 ± 0.38	67.58 ± 0.44	67.60 ± 0.37	68.05 ± 0.40
ω_{cdm}	0.11983 ± 0.00085	0.11894 ± 0.00097	0.11888 ± 0.00082	0.11790 ± 0.00089
ω_b	0.02216 ± 0.00013	0.02223 ± 0.00014	0.02223 ± 0.00013	0.02232 ± 0.00013
H_0 Tension	5.3σ	4.8σ	4.9σ	4.5σ

Table 5: The posterior central values and corresponding 68% C.L. intervals for the cosmological parameters in the Λ CDM model, along with the H_0 tension values from Eq. (3.3). The results are presented for \mathcal{B} and $\mathcal{B}_{\mathbf{EE}}$ in combination with the \mathbf{BAO} and the $\mathbf{BAO}_{\mathbf{DES}}\mathbf{I}$ datasets, as shown in Figure 6.

	$\mathcal{B}+\mathbf{BAO}+\mathbf{H}_0$	$\mathcal{B}_{\mathbf{EE}}+\mathbf{BAO}+\mathbf{H}_0$
$\log(10^{10} A_s)$	3.059 ± 0.014	3.118 ± 0.023
n_s	0.9677 ± 0.0035	0.9715 ± 0.0038
τ_{reio}	$0.0626^{+0.0071}_{-0.0082}$	0.097 ± 0.013
H_0 [km/s/Mpc]	68.04 ± 0.36	68.53 ± 0.38
ω_{cdm}	0.11805 ± 0.00080	0.11695 ± 0.00086
ω_b	0.02235 ± 0.00012	0.02243 ± 0.00012
H_0 Tension	4.6σ	4.1σ

Table 6: The posterior central values and corresponding 68% C.L. intervals for the cosmological parameters in the Λ CDM model, along with the H_0 tension values from Eq. (3.3). The results are presented for \mathcal{B} and $\mathcal{B}_{\mathbf{EE}}$ in combination with $\mathbf{BAO}+\mathbf{H}_0$ dataset, as shown in Figure 7.

	$\mathcal{B}+\mathbf{BAO}$	$\mathcal{B}_{\mathbf{EE}}+\mathbf{BAO}$	$\mathcal{B}+\mathbf{BAO}_{\mathbf{DES}}\mathbf{I}$	$\mathcal{B}_{\mathbf{EE}}+\mathbf{BAO}_{\mathbf{DES}}\mathbf{I}$
$\log(10^{10} A_s)$	3.041	3.098	3.056	3.110
n_s	0.9638	0.9643	0.9643	0.9684
τ_{reio}	0.0505	0.0851	0.0551	0.0938
H_0 [km/s/Mpc]	67.31	67.57	67.82	68.07
ω_{cdm}	0.11959	0.11905	0.11824	0.11800
ω_b	0.02218	0.02225	0.02224	0.02236

Table 7: The best-fit values for the cosmological parameters in the Λ CDM model. The results are presented for \mathcal{B} and $\mathcal{B}_{\mathbf{EE}}$ in combination with the \mathbf{BAO} and the $\mathbf{BAO}_{\mathbf{DES}}\mathbf{I}$ datasets.

	$\mathcal{B}+\mathbf{BAO}+\mathbf{H}_0$	$\mathcal{B}_{\mathbf{EE}}+\mathbf{BAO}+\mathbf{H}_0$
$\log(10^{10} A_s)$	3.061	3.115
n_s	0.9693	0.9716
τ_{reio}	0.0576	0.0953
H_0 [km/s/Mpc]	68.29	68.45
ω_{cdm}	0.11754	0.11715
ω_b	0.02235	0.02243

Table 8: The best-fit values for the cosmological parameters in the Λ CDM model. The results are presented for \mathcal{B} and $\mathcal{B}_{\mathbf{EE}}$ in combination with $\mathbf{BAO}+\mathbf{H}_0$ dataset.

	$\mathcal{B}+\mathbf{BAO}$	$\mathcal{B}_{\mathbf{EE}}+\mathbf{BAO}$	$\mathcal{B}+\mathbf{BAO}_{\text{DESI}}$	$\mathcal{B}_{\mathbf{EE}}+\mathbf{BAO}_{\text{DESI}}$
Planck lowl TT	23.2	24.7	23.3	24.2
Planck lowl EE	395.7	–	396.2	–
Planck highl TTTEEE	10543.7	10541.6	10544.2	10542.4
ACT/Planck Lensing	22.9	22.0	22.7	21.9
BAO 6dF	0.07	0.03	–	–
BAO SDSS DR7 MGS	1.0	1.2	–	–
BAO SDSS DR12	5.2	4.4	–	–
SN Pantheon+	1403.8	1404.2	1404.8	1405.2
BAO DESI	–	–	15.8	14.8
χ_{total}^2	12395.7	11998.2	12407.1	12008.7

Table 9: The contribution to the effective χ^2 from each likelihood when fitting the Λ CDM model to \mathcal{B} and $\mathcal{B}_{\mathbf{EE}}$ in combination with the \mathbf{BAO} and the $\mathbf{BAO}_{\text{DESI}}$ datasets. Shorthand notations for the likelihoods are given in Table 29.

	$\mathcal{B}+\mathbf{BAO}+\mathbf{H}_0$	$\mathcal{B}_{\mathbf{EE}}+\mathbf{BAO}+\mathbf{H}_0$
Planck lowl TT	22.4	23.6
Planck lowl EE	396.6	–
Planck highl TTTEEE	10547.3	10544.5
ACT/Planck Lensing	22.6	22.1
BAO 6dF	0.01	0.02
BAO SDSS DR7 MGS	2.0	2.2
BAO SDSS DR12	3.4	3.4
SN Pantheon+SH0ES	1486.7	1485.4
χ_{total}^2	12481.1	12081.2

Table 10: The contribution to the effective χ^2 from each likelihood when fitting the Λ CDM model to \mathcal{B} and $\mathcal{B}_{\mathbf{EE}}$ in combination with the \mathbf{H}_0 dataset. Shorthand notations for the likelihoods are given in Table 29.

A.2 Dark Radiation

A.2.1 FSDR

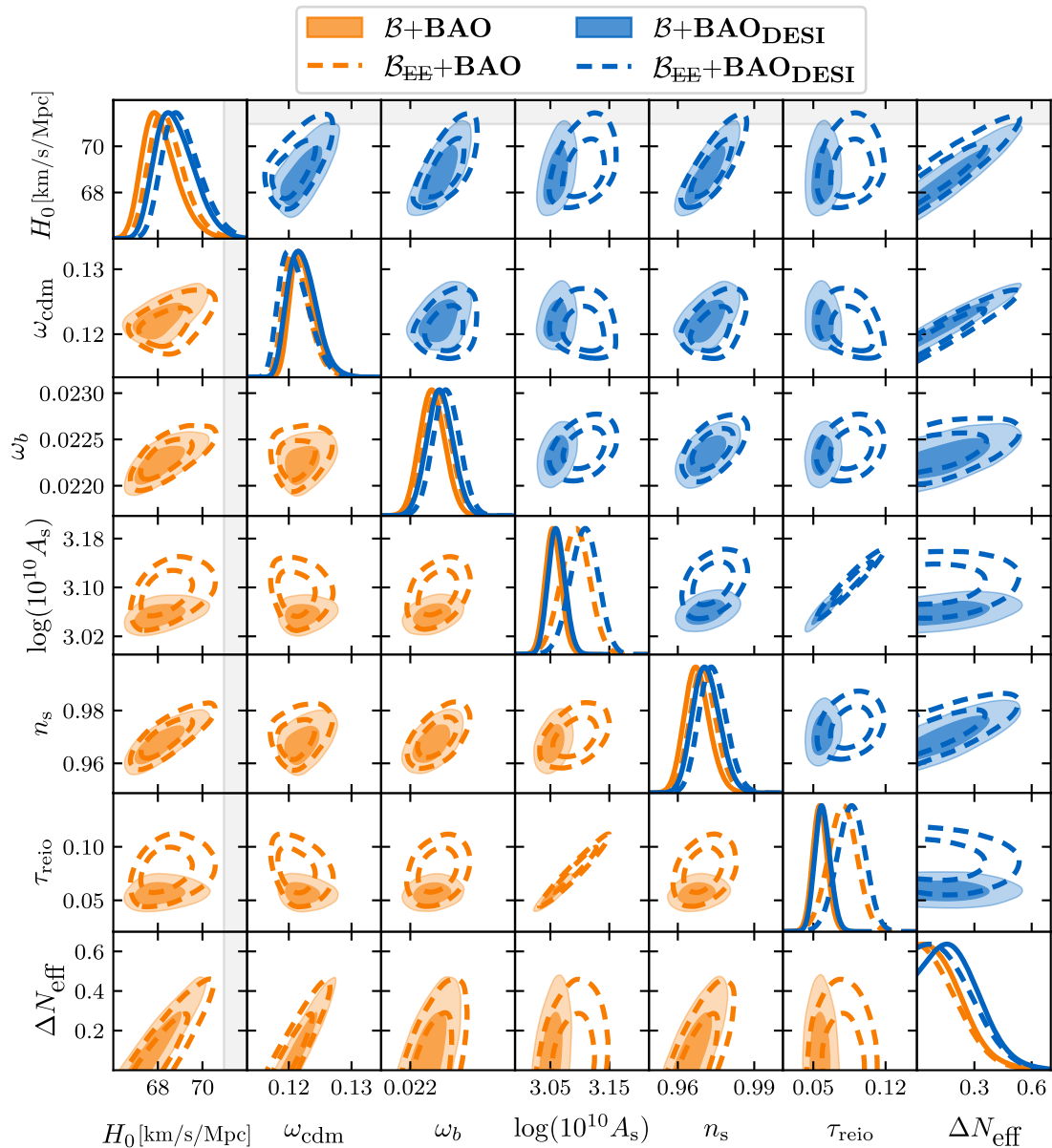


Figure 8: Posterior distributions of the cosmological parameters in the FSDR model along with its new physics parameter, ΔN_{eff} . The results from the **BAO** (**BAO_{DESI}**) dataset are shown in the lower-left (upper-right) part of the plot as orange (blue) contours. Solid (dashed) contours represent the results obtained from the \mathcal{B} (\mathcal{B}_{EE}) dataset. The gray shaded area shows the 2σ range of H_0 from the SH0ES measurement.

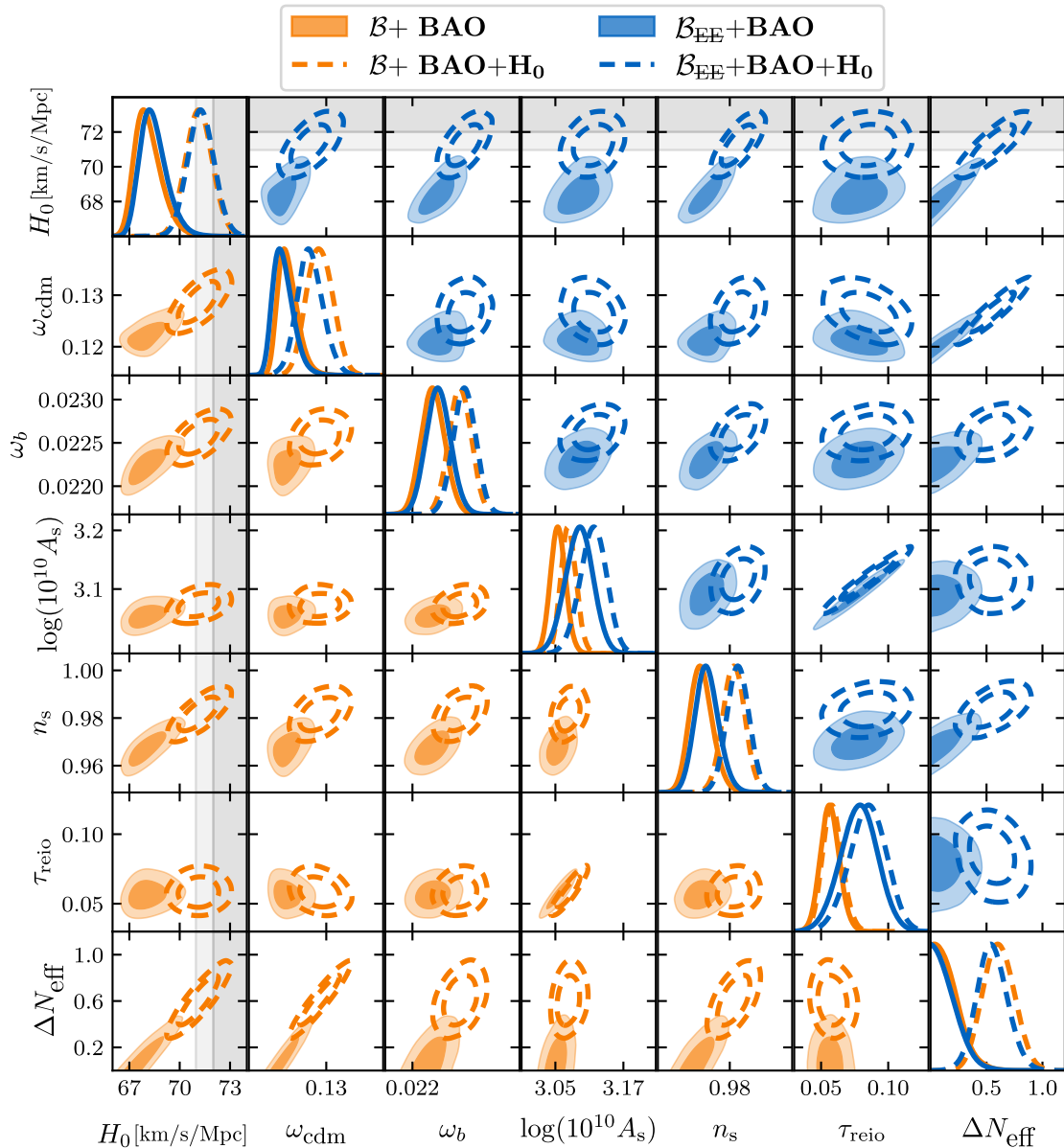


Figure 9: Posterior distributions of the cosmological parameters in the FSDR model along with its new physics parameter, ΔN_{eff} . The orange (blue) contours show the $\mathcal{B}+\text{BAO}$ ($\mathcal{B}_{\text{EE}}+\text{BAO}$) dataset. In dashed contours, the \mathbf{H}_0 dataset is included, pulling the posteriors to the high H_0 region. The gray shaded area shows the 1σ (dark gray) and 2σ (light gray) range of H_0 from the SH0ES measurement.

	$\mathcal{B}+\mathbf{BAO}$	$\mathcal{B}_{\mathbf{EE}}+\mathbf{BAO}$	$\mathcal{B}+\mathbf{BAO}_{\mathbf{DESI}}$	$\mathcal{B}_{\mathbf{EE}}+\mathbf{BAO}_{\mathbf{DESI}}$
$\log(10^{10} A_s)$	3.055 ± 0.014	3.092 ± 0.024	$3.061^{+0.013}_{-0.015}$	3.107 ± 0.023
n_s	$0.9676^{+0.0044}_{-0.0053}$	$0.9701^{+0.0047}_{-0.0054}$	$0.9712^{+0.0048}_{-0.0057}$	$0.9738^{+0.0049}_{-0.0056}$
τ_{reio}	0.0566 ± 0.0071	0.078 ± 0.014	$0.0591^{+0.0067}_{-0.0078}$	0.086 ± 0.013
H_0 [km/s/Mpc]	$68.13^{+0.58}_{-0.92}$	$68.45^{+0.60}_{-0.91}$	$68.80^{+0.69}_{-1.0}$	$69.12^{+0.65}_{-1.0}$
ω_{cdm}	$0.1223^{+0.0014}_{-0.0023}$	$0.1214^{+0.0015}_{-0.0024}$	$0.1222^{+0.0018}_{-0.0026}$	$0.1210^{+0.0018}_{-0.0028}$
ω_b	0.02225 ± 0.00014	0.02231 ± 0.00014	0.02233 ± 0.00015	0.02241 ± 0.00015
ΔN_{eff}	< 0.376	< 0.370	$0.206^{+0.064}_{-0.19}$	< 0.436
H_0 Tension	4.1σ	3.8σ	3.4σ	3.2σ

Table 11: The posterior central values and corresponding 68% C.L. intervals for the cosmological parameters in the FSDR model, along with its new physics parameter ΔN_{eff} and H_0 tension values from Eq. (3.3). The results are presented for \mathcal{B} and $\mathcal{B}_{\mathbf{EE}}$ in combination with the \mathbf{BAO} and the $\mathbf{BAO}_{\mathbf{DESI}}$ datasets, as shown in Figure 8. For ΔN_{eff} , the 95% C.L. upper bounds are provided only when a credible 68% interval away from zero is not obtained.

	$\mathcal{B}+\mathbf{BAO}+\mathbf{H}_0$	$\mathcal{B}_{\mathbf{EE}}+\mathbf{BAO}+\mathbf{H}_0$
$\log(10^{10} A_s)$	3.073 ± 0.014	3.117 ± 0.023
n_s	0.9818 ± 0.0048	0.9836 ± 0.0049
τ_{reio}	$0.0586^{+0.0067}_{-0.0077}$	0.085 ± 0.014
H_0 [km/s/Mpc]	71.15 ± 0.79	71.26 ± 0.78
ω_{cdm}	0.1287 ± 0.0026	$0.1268^{+0.0024}_{-0.0027}$
ω_b	0.02257 ± 0.00013	0.02262 ± 0.00013
ΔN_{eff}	0.61 ± 0.14	0.55 ± 0.14
H_0 Tension	1.5σ	1.4σ

Table 12: The posterior central values and corresponding 68% C.L. intervals for the cosmological parameters in the FSDR model, along with its new physics parameter ΔN_{eff} and H_0 tension values from Eq. (3.3). The results are presented for \mathcal{B} and $\mathcal{B}_{\mathbf{EE}}$ in combination with $\mathbf{BAO}+\mathbf{H}_0$ dataset, as shown in Figure 9.

	$\mathcal{B}+\mathbf{BAO}$	$\mathcal{B}_{\mathbf{EE}}+\mathbf{BAO}$	$\mathcal{B}+\mathbf{BAO}_{\mathbf{DESI}}$	$\mathcal{B}_{\mathbf{EE}}+\mathbf{BAO}_{\mathbf{DESI}}$
$\log(10^{10} A_s)$	3.057	3.103	3.046	3.114
n_s	0.9673	0.9673	0.9673	0.9740
τ_{reio}	0.0540	0.0875	0.0504	0.0885
H_0 [km/s/Mpc]	68.34	67.85	68.22	69.33
ω_{cdm}	0.12208	0.11930	0.12080	0.12140
ω_b	0.02223	0.02227	0.02223	0.02241
ΔN_{eff}	0.17	0.03	0.11	0.23
$\chi^2 - \chi^2_{\Lambda\text{CDM}}$	-0.6	+0.0	+0.3	+0.3

Table 13: The best-fit values for the cosmological parameters in the FSDR model, along with its new physics parameter ΔN_{eff} . The results are presented for \mathcal{B} and $\mathcal{B}_{\mathbf{EE}}$ in combination with the \mathbf{BAO} and the $\mathbf{BAO}_{\mathbf{DESI}}$ datasets. The χ^2 differences with respect to the corresponding ΛCDM cases are also presented.

Parameter	$\mathcal{B}+\mathbf{BAO}+\mathbf{H}_0$	$\mathcal{B}_{\mathbf{EE}}+\mathbf{BAO}+\mathbf{H}_0$
$\log(10^{10} A_s)$	3.077	3.115
n_s	0.9804	0.9817
τ_{reio}	0.0566	0.0823
H_0 [km/s/Mpc]	71.28	71.14
ω_{cdm}	0.12873	0.12642
ω_b	0.02256	0.02258
ΔN_{eff}	0.63	0.53
$\chi^2 - \chi_{\Lambda\text{CDM}}^2$	-21.1	-18.8

Table 14: The best-fit values for the cosmological parameters in the FSDR model, along with its new physics parameter ΔN_{eff} . The results are presented for \mathcal{B} and $\mathcal{B}_{\mathbf{EE}}$ in combination with $\mathbf{BAO}+\mathbf{H}_0$ dataset. The χ^2 differences with respect to the corresponding ΛCDM cases are also presented.

	$\mathcal{B}+\mathbf{BAO}$	$\mathcal{B}_{\mathbf{EE}}+\mathbf{BAO}$	$\mathcal{B}+\mathbf{BAO}_{\text{DESI}}$	$\mathcal{B}_{\mathbf{EE}}+\mathbf{BAO}_{\text{DESI}}$
Planck lowl TT	23.0	24.2	22.7	23.2
Planck lowl EE	396.1	–	395.8	–
Planck highl TTTEEE	10543.9	10542.2	10544.3	10543.9
ACT/Planck Lensing	22.1	21.9	23.2	22.1
BAO 6dF	0.03	0.01	–	–
BAO SDSS DR7 MGS	1.3	1.4	–	–
BAO SDSS DR12	4.4	4.0	–	–
SN Pantheon+	1404.3	1404.5	1404.6	1405.9
BAO DESI	–	–	16.8	13.9
χ_{total}^2	12395.1	11998.1	12407.4	12009.0

Table 15: The contribution to the effective χ^2 from each likelihood when fitting the FSDR model to \mathcal{B} and $\mathcal{B}_{\mathbf{EE}}$ in combination with the \mathbf{BAO} and the $\mathbf{BAO}_{\text{DESI}}$ datasets. Shorthand notations for the likelihoods are given in Table 29.

	$\mathcal{B}+\mathbf{BAO}+\mathbf{H}_0$	$\mathcal{B}_{\mathbf{EE}}+\mathbf{BAO}+\mathbf{H}_0$
Planck lowl TT	21.6	22.2
Planck lowl EE	396.5	–
Planck highl TTTEEE	10552.1	10548.7
ACT/Planck Lensing	22.2	22.0
BAO 6dF	0.01	0.04
BAO SDSS DR7 MGS	2.1	2.4
BAO SDSS DR12	3.5	3.6
SN Pantheon+SH0ES	1461.8	1463.5
χ_{total}^2	12460.0	12062.4

Table 16: The contribution to the effective χ^2 from each likelihood when fitting the FSDR model to \mathcal{B} and $\mathcal{B}_{\mathbf{EE}}$ in combination with the \mathbf{H}_0 dataset. Shorthand notations for the likelihoods are given in Table 29.

A.2.2 SIDR

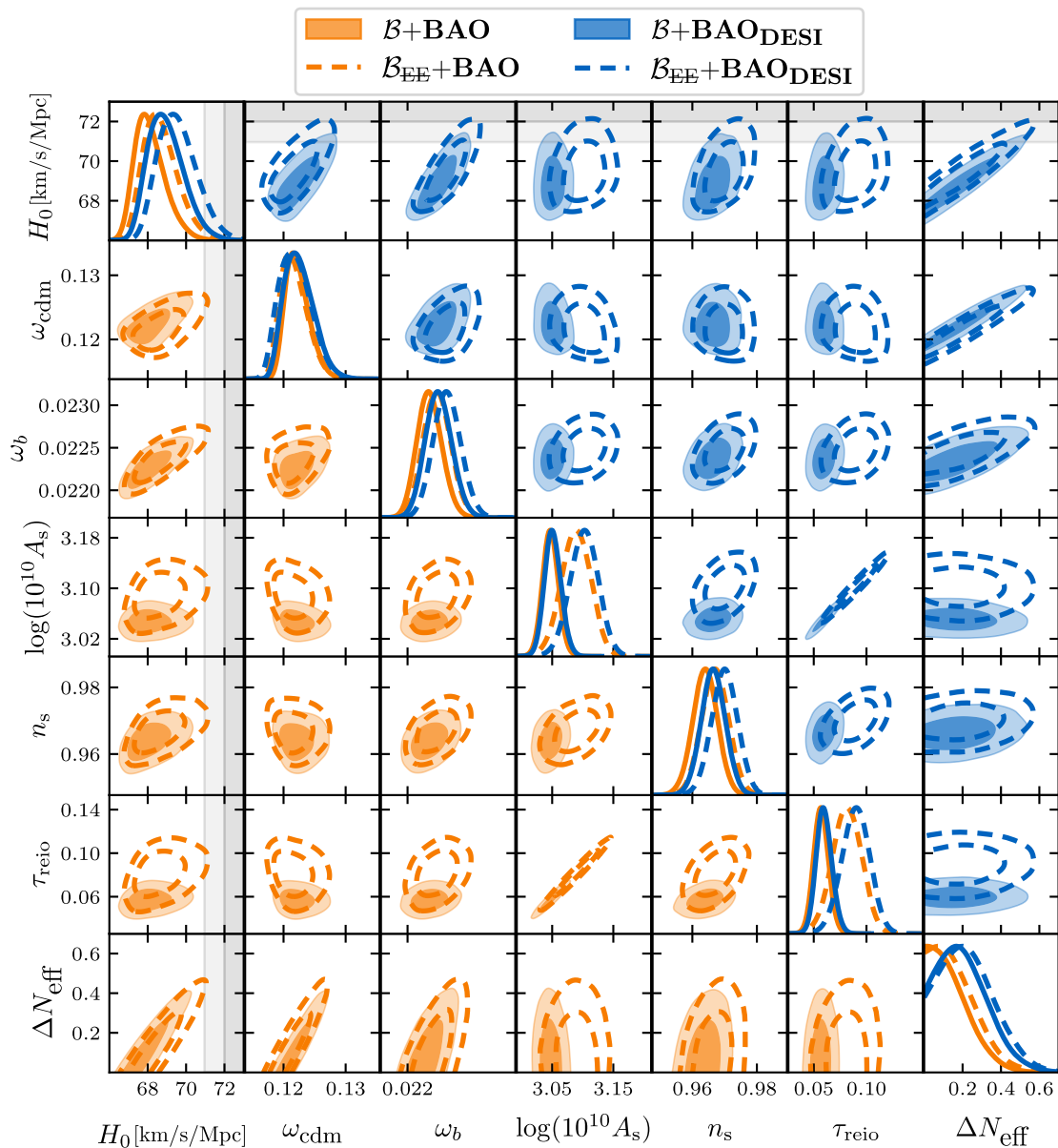


Figure 10: Posterior distributions of the cosmological parameters in the SIDR model along with its new physics parameter, ΔN_{eff} . The results from the **BAO** (**BAO_{DES}**) dataset are shown in the lower-left (upper-right) part of the plot as orange (blue) contours. Solid (dashed) contours represent the results obtained from the \mathcal{B} (\mathcal{B}_{EE}) dataset. The gray shaded area shows the 1σ (dark gray) and 2σ (light gray) range of H_0 from the SH0ES measurement.

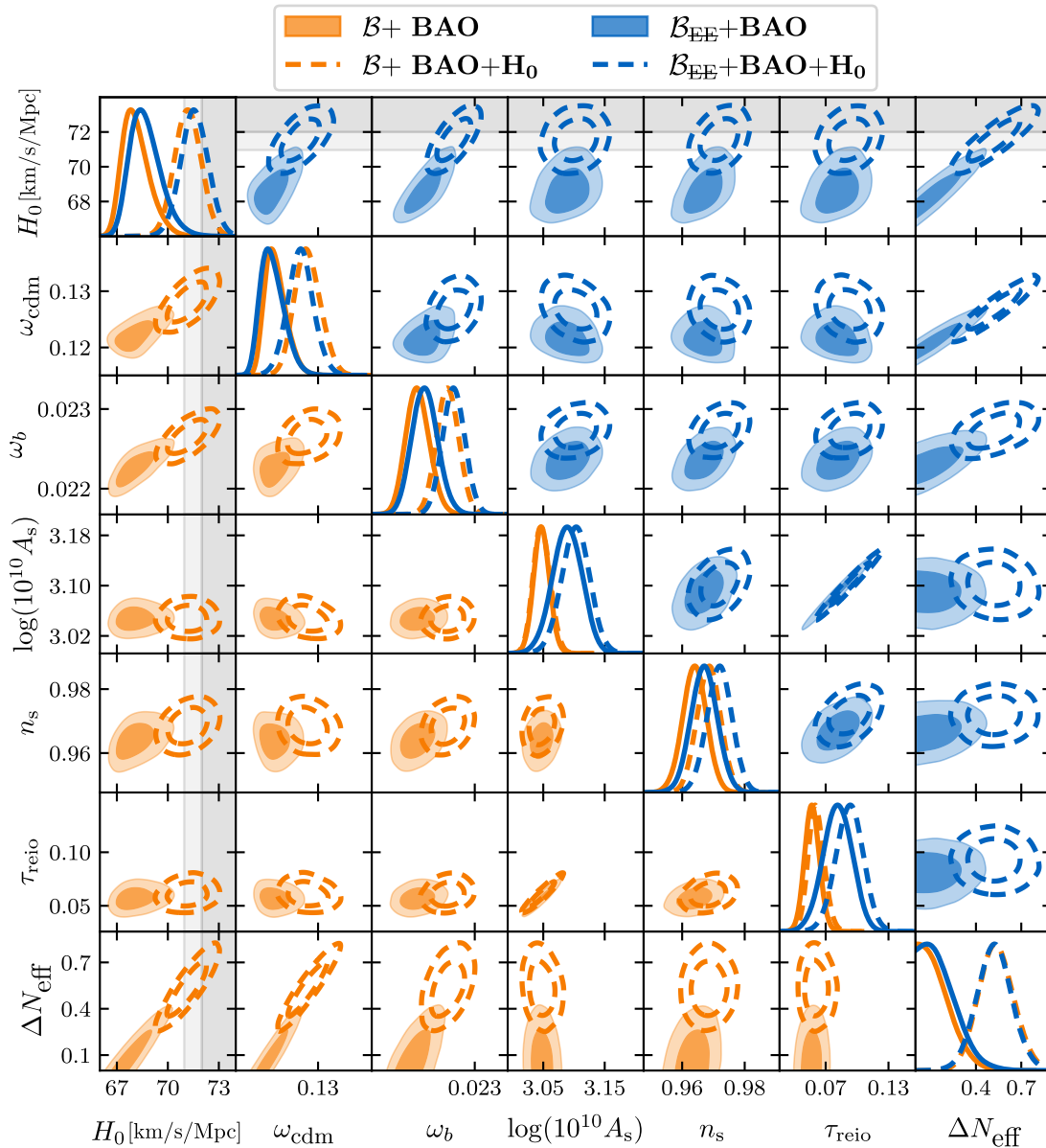


Figure 11: Posterior distributions of the cosmological parameters in the SIDR model along with its new physics parameter, ΔN_{eff} . The orange (blue) contours show the $\mathcal{B} + \text{BAO}$ ($\mathcal{B}_{\text{EE}} + \text{BAO}$) dataset. In dashed contours, the \mathbf{H}_0 dataset is included, pulling the posteriors to the high H_0 region. The gray shaded area shows the 1σ (dark gray) and 2σ (light gray) range of H_0 from the SH0ES measurement.

	$\mathcal{B}+\text{BAO}$	$\mathcal{B}_{\text{EE}}+\text{BAO}$	$\mathcal{B}+\text{BAO}_{\text{DES}}I$	$\mathcal{B}_{\text{EE}}+\text{BAO}_{\text{DES}}I$
$\log(10^{10} A_s)$	3.047 ± 0.013	3.089 ± 0.024	3.051 ± 0.014	3.102 ± 0.023
n_s	0.9640 ± 0.0038	0.9670 ± 0.0042	0.9665 ± 0.0037	0.9700 ± 0.0040
τ_{reio}	0.0570 ± 0.0071	0.081 ± 0.014	$0.0599^{+0.0068}_{-0.0078}$	0.090 ± 0.013
H_0 [km/s/Mpc]	$68.14^{+0.59}_{-0.94}$	$68.69^{+0.69}_{-1.1}$	$68.95^{+0.74}_{-1.1}$	$69.55^{+0.82}_{-1.2}$
ω_{cdm}	$0.1223^{+0.0014}_{-0.0023}$	$0.1217^{+0.0016}_{-0.0025}$	$0.1225^{+0.0019}_{-0.0028}$	$0.1219^{+0.0021}_{-0.0029}$
ω_b	$0.02227^{+0.00014}_{-0.00016}$	0.02236 ± 0.00016	0.02238 ± 0.00016	0.02248 ± 0.00017
ΔN_{eff}	< 0.340	< 0.380	$0.206^{+0.078}_{-0.18}$	$0.228^{+0.096}_{-0.18}$
H_0 Tension	4.1σ	3.5σ	3.2σ	2.6σ

Table 17: The posterior central values and corresponding 68% C.L. intervals for the cosmological parameters in the SIDR model, along with its new physics parameter ΔN_{eff} and H_0 tension values from Eq. (3.3). The results are presented for \mathcal{B} and \mathcal{B}_{EE} in combination with the **BAO** and the **BAO_{DES}I** datasets, as shown in Figure 10. For ΔN_{eff} , the 95% C.L. upper bounds are provided only when a credible 68% interval away from zero is not obtained.

	$\mathcal{B}+\text{BAO}+\text{H}_0$	$\mathcal{B}_{\text{EE}}+\text{BAO}+\text{H}_0$
$\log(10^{10} A_s)$	$3.048^{+0.013}_{-0.015}$	3.102 ± 0.023
n_s	0.9685 ± 0.0037	0.9719 ± 0.0040
τ_{reio}	$0.0611^{+0.0069}_{-0.0080}$	0.093 ± 0.013
H_0 [km/s/Mpc]	71.17 ± 0.77	71.57 ± 0.80
ω_{cdm}	$0.1281^{+0.0022}_{-0.0025}$	0.1268 ± 0.0024
ω_b	0.02265 ± 0.00014	0.02273 ± 0.00014
ΔN_{eff}	0.53 ± 0.12	0.52 ± 0.12
H_0 Tension	1.5σ	1.1σ

Table 18: The posterior central values and corresponding 68% C.L. intervals for the cosmological parameters in the SIDR model, along with its new physics parameter ΔN_{eff} and H_0 tension values from Eq. (3.3). The results are presented for \mathcal{B} and \mathcal{B}_{EE} in combination with **BAO+H₀** dataset, as shown in Figure 11.

	$\mathcal{B}+\text{BAO}$	$\mathcal{B}_{\text{EE}}+\text{BAO}$	$\mathcal{B}+\text{BAO}_{\text{DES}}I$	$\mathcal{B}_{\text{EE}}+\text{BAO}_{\text{DES}}I$
$\log(10^{10} A_s)$	3.055	3.093	3.043	3.101
n_s	0.9639	0.9675	0.9670	0.9705
τ_{reio}	0.0577	0.0868	0.0476	0.0893
H_0 [km/s/Mpc]	67.97	68.98	69.38	70.09
ω_{cdm}	0.12222	0.12230	0.12222	0.12370
ω_b	0.02222	0.02241	0.02242	0.02251
ΔN_{eff}	0.11	0.20	0.23	0.33
$\chi^2 - \chi^2_{\Lambda\text{CDM}}$	-1.0	+0.1	-2.9	-1.8

Table 19: The best-fit values for the cosmological parameters in the SIDR model, along with its new physics parameter ΔN_{eff} . The results are presented for \mathcal{B} and \mathcal{B}_{EE} in combination with the **BAO** and the **BAO_{DES}I** datasets. The χ^2 differences with respect to the corresponding ΛCDM cases are also presented.

	$\mathcal{B}+\mathbf{BAO}+\mathbf{H}_0$	$\mathcal{B}_{\mathbf{EE}}+\mathbf{BAO}+\mathbf{H}_0$
$\log(10^{10} A_s)$	3.040	3.093
n_s	0.9702	0.9701
τ_{reio}	0.0534	0.0861
H_0 [km/s/Mpc]	71.75	71.83
ω_{cdm}	0.12916	0.12841
ω_b	0.02268	0.02275
ΔN_{eff}	0.61	0.59
$\chi^2 - \chi_{\Lambda\text{CDM}}^2$	-24.1	-23.1

Table 20: The best-fit values for the cosmological parameters in the SIDR model, along with its new physics parameter ΔN_{eff} . The results are presented for \mathcal{B} and $\mathcal{B}_{\mathbf{EE}}$ in combination with $\mathbf{BAO}+\mathbf{H}_0$ dataset. The χ^2 differences with respect to the corresponding ΛCDM cases are also presented.

	$\mathcal{B}+\mathbf{BAO}$	$\mathcal{B}_{\mathbf{EE}}+\mathbf{BAO}$	$\mathcal{B}+\mathbf{BAO}_{\text{DESI}}$	$\mathcal{B}_{\mathbf{EE}}+\mathbf{BAO}_{\text{DESI}}$
Planck lowl TT	23.4	23.9	22.4	23.2
Planck lowl EE	397.0	–	395.8	–
Planck highl TTTEEE	10542.2	10541.8	10543.4	10542.0
ACT/Planck Lensing	22.1	22.3	22.8	22.2
BAO 6dF	0.05	0.00	–	–
BAO SDSS DR7 MGS	1.1	1.7	–	–
BAO SDSS DR12	4.8	3.6	–	–
SN Pantheon+	1404.0	1405.0	1405.7	1406.3
BAO DESI	–	–	14.0	13.3
χ_{total}^2	12394.7	11998.2	12404.1	12006.8

Table 21: The contribution to the effective χ^2 from each likelihood when fitting the SIDR model to \mathcal{B} and $\mathcal{B}_{\mathbf{EE}}$ in combination with the \mathbf{BAO} and the $\mathbf{BAO}_{\text{DESI}}$ datasets. Shorthand notations for the likelihoods are given in Table 29.

	$\mathcal{B}+\mathbf{BAO}+\mathbf{H}_0$	$\mathcal{B}_{\mathbf{EE}}+\mathbf{BAO}+\mathbf{H}_0$
Planck lowl TT	21.9	23.0
Planck lowl EE	396.0	–
Planck highl TTTEEE	10549.1	10545.2
ACT/Planck Lensing	23.6	22.7
BAO 6dF	0.05	0.08
BAO SDSS DR7 MGS	2.4	2.6
BAO SDSS DR12	3.7	3.9
SN Pantheon+SH0ES	1460.4	1460.6
χ_{total}^2	12457.0	12058.1

Table 22: The contribution to the effective χ^2 from each likelihood when fitting the SIDR model to \mathcal{B} and $\mathcal{B}_{\mathbf{EE}}$ in combination with the \mathbf{H}_0 dataset. Shorthand notations for the likelihoods are given in Table 29.

A.3 Early Dark Energy

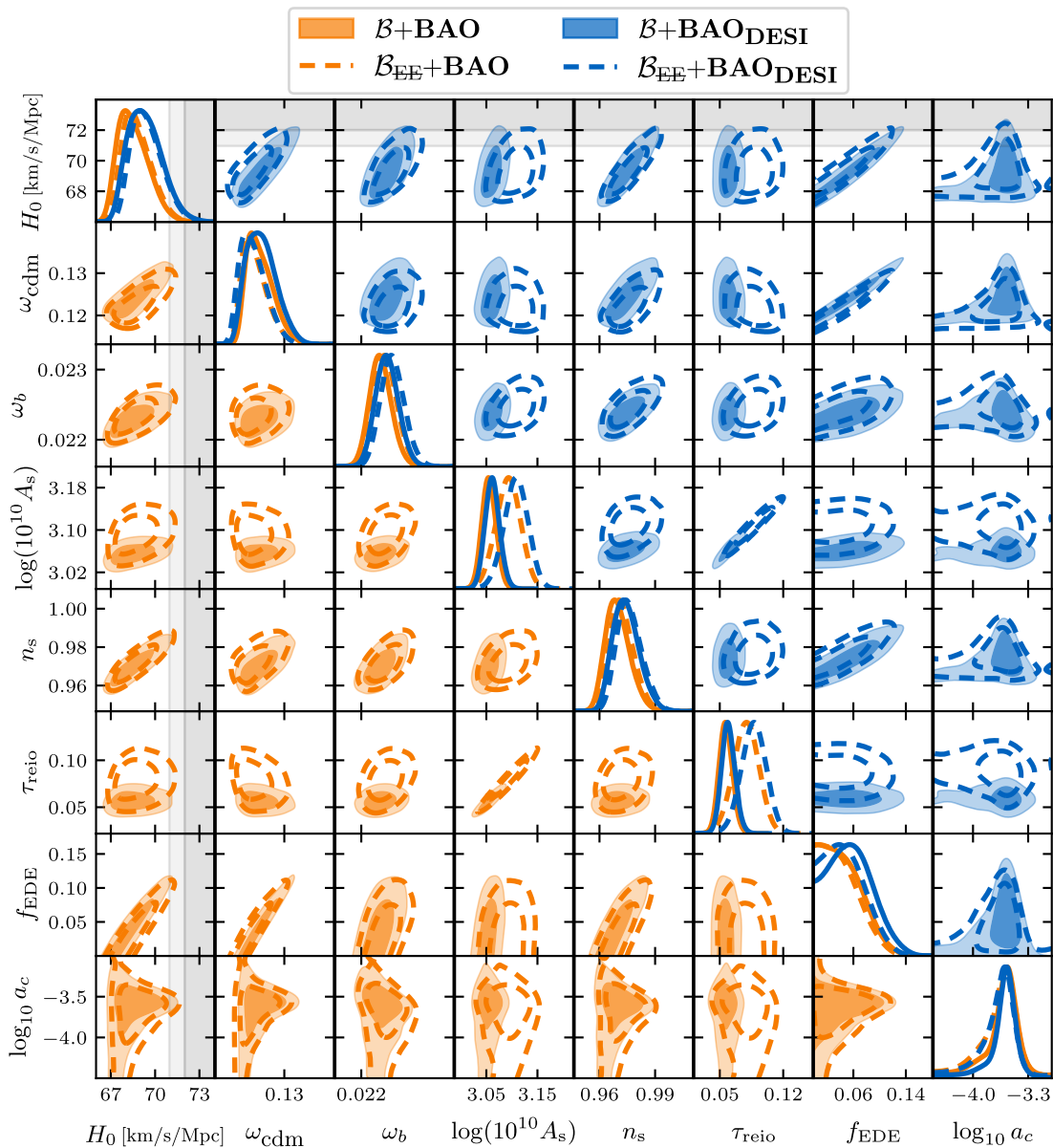


Figure 12: Posterior distributions of the cosmological parameters in the EDE model, along with its new physics parameters, $\{f_{\text{EDE}}, a_c\}$. The results from the **BAO** (**BAO_{DESI}**) dataset are shown in the lower-left (upper-right) part of the plot as orange (blue) contours. Solid (dashed) contours represent the results obtained from the \mathcal{B} (\mathcal{B}_{EE}) dataset. The gray shaded area shows the 1σ (dark gray) and 2σ (light gray) range of H_0 from the SH0ES measurement.

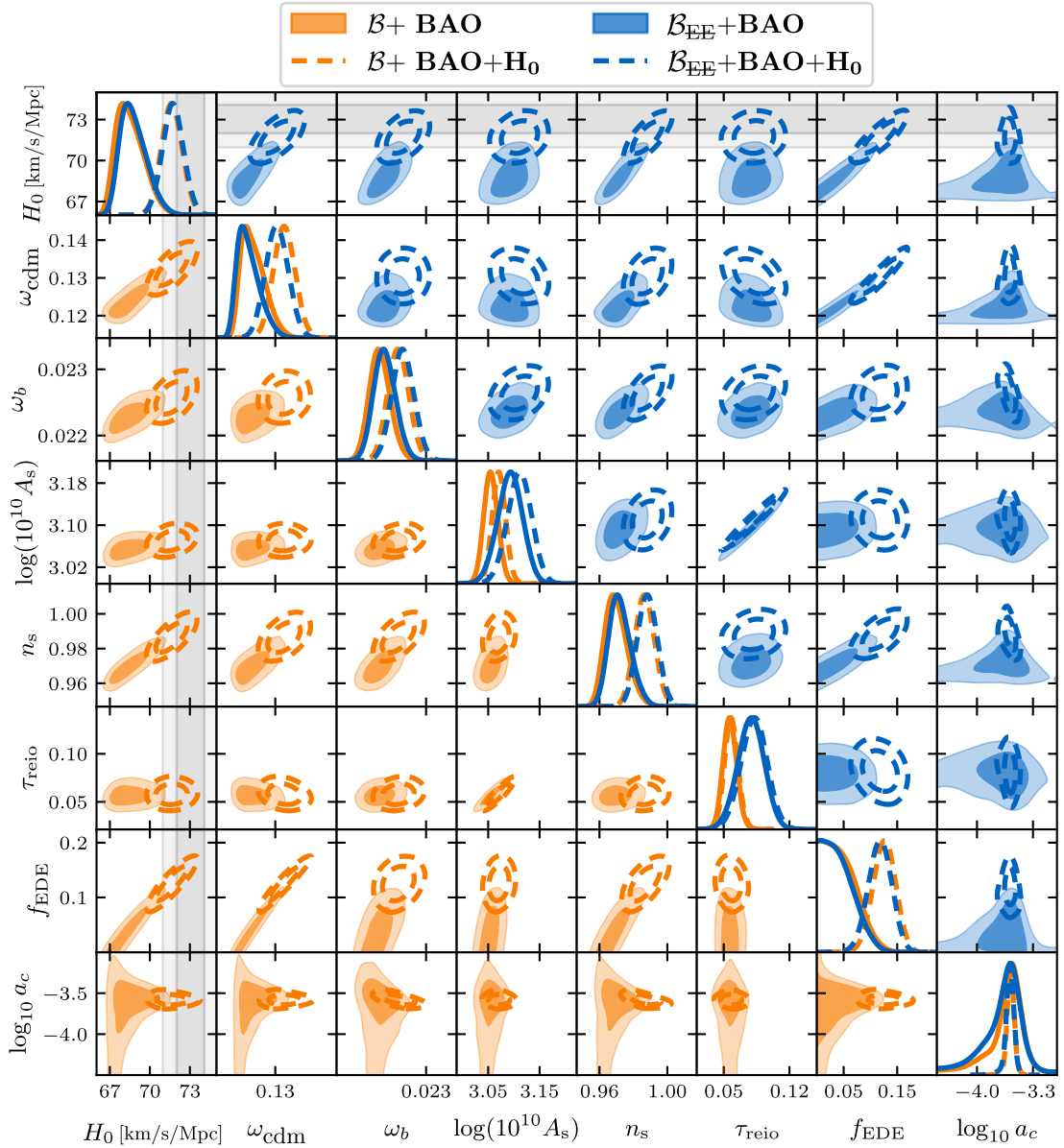


Figure 13: Posterior distributions of the cosmological parameters in the EDE model, along with its new physics parameters, $\{f_{\text{EDE}}, a_c\}$. The orange (blue) contours show the $\mathcal{B}+\text{BAO}$ ($\mathcal{B}_{\text{EE}}+\text{BAO}$) dataset. In dashed contours, the \mathbf{H}_0 dataset is included, pulling the posteriors to the high H_0 region. The gray shaded area shows the 1σ (dark gray) and 2σ (light gray) range of H_0 from the SH0ES measurement.

	$\mathcal{B}+\text{BAO}$	$\mathcal{B}_{\text{EE}}+\text{BAO}$	$\mathcal{B}+\text{BAO}_{\text{DESI}}$	$\mathcal{B}_{\text{EE}}+\text{BAO}_{\text{DESI}}$
$\log(10^{10} A_s)$	3.055 ± 0.014	3.093 ± 0.024	3.062 ± 0.014	3.108 ± 0.023
n_s	$0.9699^{+0.0054}_{-0.0074}$	$0.9721^{+0.0054}_{-0.0072}$	$0.9744^{+0.0059}_{-0.0079}$	$0.9762^{+0.0056}_{-0.0077}$
H_0 [km/s/Mpc]	$68.52^{+0.77}_{-1.2}$	$68.78^{+0.74}_{-1.2}$	$69.32^{+0.92}_{-1.3}$	$69.43^{+0.80}_{-1.2}$
τ_{reio}	0.0566 ± 0.0073	0.079 ± 0.014	$0.0594^{+0.0069}_{-0.0077}$	0.087 ± 0.014
ω_{cdm}	$0.1240^{+0.0022}_{-0.0039}$	$0.1228^{+0.0020}_{-0.0036}$	$0.1244^{+0.0028}_{-0.0043}$	$0.1224^{+0.0023}_{-0.0039}$
ω_b	$0.02229^{+0.00015}_{-0.00017}$	$0.02236^{+0.00016}_{-0.00018}$	$0.02238^{+0.00016}_{-0.00018}$	$0.02246^{+0.00016}_{-0.00019}$
f_{EDE}	< 0.0977	< 0.0924	$0.056^{+0.028}_{-0.041}$	$0.048^{+0.016}_{-0.045}$
$\log_{10} a_c$	$-3.64^{+0.25}_{-0.11}$	$-3.68^{+0.27}_{-0.15}$	$-3.62^{+0.19}_{-0.081}$	$-3.68^{+0.24}_{-0.13}$
H_0 Tension	3.5σ	3.3σ	2.7σ	2.8σ

Table 23: The posterior central values and corresponding 68% C.L. intervals for the cosmological parameters in the EDE model, along with its new physics parameters $\{f_{\text{EDE}}, a_c\}$ and H_0 tension values from Eq. (3.3). The results are presented for \mathcal{B} and \mathcal{B}_{EE} in combination with the **BAO** and the **BAO_{DESI}** datasets, as shown in Figure 12. For f_{EDE} , the 95% C.L. upper bounds are provided only when a credible 68% interval away from zero is not obtained.

	$\mathcal{B}+\text{BAO}+\text{H}_0$	$\mathcal{B}_{\text{EE}}+\text{BAO}+\text{H}_0$
$\log(10^{10} A_s)$	3.071 ± 0.013	3.111 ± 0.023
n_s	0.9866 ± 0.0058	0.9882 ± 0.0058
H_0 [km/s/Mpc]	71.64 ± 0.78	71.73 ± 0.79
τ_{reio}	0.0581 ± 0.0073	0.082 ± 0.014
ω_{cdm}	0.1324 ± 0.0029	0.1304 ± 0.0031
ω_b	0.02257 ± 0.00016	0.02264 ± 0.00017
f_{EDE}	0.126 ± 0.021	0.118 ± 0.022
$\log_{10} a_c$	-3.580 ± 0.046	$-3.591^{+0.051}_{-0.042}$
H_0 Tension	1.1σ	1.0σ

Table 24: The posterior central values and corresponding 68% C.L. intervals for the cosmological parameters in the EDE model, along with its new physics parameters $\{f_{\text{EDE}}, a_c\}$ and H_0 tension values from Eq. (3.3). The results are presented for \mathcal{B} and \mathcal{B}_{EE} in combination with **BAO+H₀** dataset, as shown in Figure 13.

	$\mathcal{B}+\mathbf{BAO}$	$\mathcal{B}_{\mathbf{EE}}+\mathbf{BAO}$	$\mathcal{B}+\mathbf{BAO}_{\mathbf{DESI}}$	$\mathcal{B}_{\mathbf{EE}}+\mathbf{BAO}_{\mathbf{DESI}}$
$\log(10^{10} A_s)$	3.062	3.086	3.062	3.126
n_s	0.972	0.974	0.976	0.979
H_0 [km/s/Mpc]	69.21	69.34	69.69	69.63
τ_{reio}	0.0550	0.0739	0.0559	0.0992
ω_{cdm}	0.12453	0.12498	0.12441	0.12387
ω_b	0.02232	0.02243	0.02233	0.02246
f_{EDE}	0.056	0.060	0.061	0.059
$\log_{10} a_c$	-3.57	-3.59	-3.52	-3.62
$\chi^2 - \chi_{\Lambda\text{CDM}}^2$	-2.0	-2.0	-1.8	-2.5

Table 25: The best-fit values for the cosmological parameters in the EDE model, along with its new physics parameters $\{f_{\text{EDE}}, a_c\}$. The results are presented for \mathcal{B} and $\mathcal{B}_{\mathbf{EE}}$ in combination with the \mathbf{BAO} and the $\mathbf{BAO}_{\mathbf{DESI}}$ datasets. The χ^2 differences with respect to the corresponding ΛCDM cases are also presented.

	$\mathcal{B}+\mathbf{BAO}+\mathbf{H}_0$	$\mathcal{B}_{\mathbf{EE}}+\mathbf{BAO}+\mathbf{H}_0$
$\log(10^{10} A_s)$	3.072	3.126
n_s	0.985	0.990
H_0 [km/s/Mpc]	71.52	71.58
τ_{reio}	0.0555	0.0963
ω_{cdm}	0.13196	0.12928
ω_b	0.02252	0.02272
f_{EDE}	0.123	0.110
$\log_{10} a_c$	-3.574	-3.610
$\chi^2 - \chi_{\Lambda\text{CDM}}^2$	-28.1	-27.0

Table 26: The best-fit values for the cosmological parameters in the EDE model, along with its new physics parameters $\{f_{\text{EDE}}, a_c\}$. The results are presented for \mathcal{B} and $\mathcal{B}_{\mathbf{EE}}$ in combination with $\mathbf{BAO}+\mathbf{H}_0$ dataset. The χ^2 differences with respect to the corresponding ΛCDM cases are also presented.

	$\mathcal{B}+\text{BAO}$	$\mathcal{B}_{\text{EE}}+\text{BAO}$	$\mathcal{B}+\text{BAO}_{\text{DESI}}$	$\mathcal{B}_{\text{EE}}+\text{BAO}_{\text{DESI}}$
Planck lowl TT	22.5	23.0	22.0	23.1
Planck lowl EE	396.2	–	396.3	–
Planck highl TTTEEE	10543.3	10541.9	10545.4	10541.9
ACT/Planck Lensing	21.6	21.3	21.5	21.2
BAO 6dF	0.01	0.01	–	–
BAO SDSS DR7 MGS	1.5	1.4	–	–
BAO SDSS DR12	3.9	4.0	–	–
SN Pantheon+	1404.7	1404.7	1405.4	1405.4
BAO DESI	–	–	14.6	14.6
χ_{total}^2	12393.7	11996.2	12405.2	12006.2

Table 27: The contribution to the effective χ^2 from each likelihood when fitting the EDE model to \mathcal{B} and \mathcal{B}_{EE} in combination with the **BAO** and the **BAO_{DESI}** datasets. Shorthand notations for the likelihoods are given in Table 29.

	$\mathcal{B}+\text{BAO}+\mathbf{H}_0$	$\mathcal{B}_{\text{EE}}+\text{BAO}+\mathbf{H}_0$
Planck lowl TT	21.4	21.7
Planck lowl EE	396.3	–
Planck highl TTTEEE	10549.2	10545.3
ACT/Planck Lensing	21.1	20.8
BAO 6dF	0.00	0.02
BAO SDSS DR7 MGS	1.8	2.2
BAO SDSS DR12	3.5	3.5
SN Pantheon+SH0ES	1460.7	1460.7
χ_{total}^2	12453.0	12054.2

Table 28: The contribution to the effective χ^2 from each likelihood when fitting the EDE model to \mathcal{B} and \mathcal{B}_{EE} in combination with the **H₀** dataset. Shorthand notations for the likelihoods are given in Table 29.

Likelihood	Shorthand
planck_2018_lowl.TT	Planck lowl TT
planck_2018_lowl.EE	Planck lowl EE
planck_NPIPE_highl_CamSpec.TTTEEE	Planck highl TTTEEE
act_dr6_lenslike.ACTDR6LensLike	ACT/Planck Lensing
bao.sixdf_2011_bao	BAO 6dF
bao.sdss_dr7_mgs	BAO SDSS DR7 MGS
bao.sdss_dr12_consensus_bao	BAO SDSS DR12
bao.desi_2024_bao_all	BAO DESI
sn.pantheonplus	SN Pantheon+
sn.pantheonplusshoes	SN Pantheon+SH0ES

Table 29: Shorthand notation used in the above tables of χ^2 values to denote specific likelihoods as implemented in Cobaya.